ABSTRACT

Title of Document: PHYSICAL MECHANISM OF TERAHERTZ GENERATION IN TWO-COLOR PHOTOIONIZATION

Yong Sing You, Doctor of Philosophy, 2014

Directed By: Professor Ki-Yong Kim
Institute for Research in Electronics and Applied Physics

Two-color photoionization has been widely used as a versatile tool for intense, broadband terahertz (THz) radiation generation. In this scheme, an ultrashort laser's fundamental and its second harmonic pulses are co-focused into a gas of atoms or molecules, transforming them into plasma by photoionization. This process produces an intense THz pulse emitted in the forward direction. The main focus of this dissertation is to provide a physical understanding of such THz generation and investigate its generation mechanism at both microscopic and macroscopic levels.

First, we examine the generation process by measuring the relative phase between two-color (fundamental and second harmonic) laser fields and the resulting THz field simultaneously. We discover that a relative phase of $\pi/2$ yields maximal THz outputs, consistent with a semi-classical plasma current model. We find that this optimal relative phase is independent of laser intensities, gas species, and two-color laser amplitude ratios. We also measure concurrent near-field photocurrents. All these

measurements verify laser-produced plasma currents as a microscopic source for THz generation.

We also investigate THz radiation from an ensemble of aligned air molecules in two-color laser fields. Our experiments show that THz radiation is strongly affected by molecular (nitrogen and oxygen) alignment. We explain this phenomenon in the context of the plasma current model combined with alignment-dependent ionization.

Phase-matching is essential to achieve high-efficiency nonlinear frequency conversion. We discover THz generation by two-color photoionization in elongated air plasmas (filamentation) is naturally phase-matched in the off-axis direction, resulting in donut-shaped radiation profiles in the far field. Because of this off-axis phase-matching, THz yields increase almost linearly with the filament length, scalable for further THz energy enhancement.

Lastly, we study the polarization of emitted THz radiation. In the case of in-line focusing geometry, we observe the polarization evolves from linear to elliptical with increasing plasma length. This ellipticity arises from two combined effects—successive polarization rotation of local THz plasma sources, caused by laser phase and polarization modulations, and the velocity mismatch between laser and THz, which produces an elliptical THz pulse from a series of time-delayed, polarization-rotating local THz fields.

PHYSICAL MECHANISM OF TERAHERTZ GENERATION IN TWO-COLOR PHOTOIONIZATION

By

Yong Sing You

Dissertation submitted to the Faculty of the Graduate School of the
University of Maryland, College Park, in partial fulfillment
of the requirements for the degree of
Doctor of Philosophy
2014

Advisory Committee:
Professor Ki-Yong Kim, Chair
Professor Edo Waks
Professor Thomas M. Antonsen, Jr.
Professor Phillip A. Sprangle
Professor Thomas E. Murphy

Dedication

Dedicated to my parents, Nam Poo and Yeok Eng, and my wife, Chian Yi

Acknowledgements

First and foremost, I want to thank my advisor, Prof. Ki-Yong Kim, for his dedicated and excellent mentorship throughout my Ph.D. training in the lab. His advices and guidance on my research are invaluable. Also, this dissertation would have been impossible without his careful reading and editing.

Throughout the years of my stay in the lab, I received a lot of help and support from my colleagues, especially Dr. Taek Il Oh, Dr. Dongwen Zhang, Inhyuk Nam, Dr. Jane Lee, Yungjun Yoo, Donggyu Jang, Jeffrey Magill, Vijay Kaul and Yan Tay. I would like to express my deepest appreciation to them. I am also grateful to Prof. Thomas Antonsen, Dr. John Palastro, Luke Johnson, and Thomas Rensink for providing excellent theoretical and simulation supports for our experiments. I would like to thank Prof. Milchberg and his group members for various kinds of help to our lab. I want to express my gratitude to all my committee members, including Prof. Antonsen, Prof. Sprangle, Prof. Murphy and Prof. Waks, for their beneficial comments and suggestions to my dissertation. Special thanks to Prof. Waks, who was willing to participate in my defense at the last moment. I would like to thank all my friends in College Park for their help and accompaniment during my stay here.

I am forever indebted to my family for supporting my decision to study Ph.D. I am grateful to my parents for their love and care all the time. I am also grateful to my brothers for their continuing encouragements. Finally, I want to thank my wife, Chian Yi, for her endless love and support.

Table of Contents

List of Figures

Chapter 1 : Terahertz Generation from Laser-Produced Plasma

1.1 Introduction to terahertz science

Terahertz (THz) radiation is electromagnetic radiation with its frequency lying between the microwave and infrared radiation regions (see Figure 1.1). It includes electromagnetic radiation from 0.1 THz to 30 THz, corresponding to wavelengths of 3 mm down to 10 μm, and periods of 10 picoseconds (ps) to 33 femtoseconds (fs).

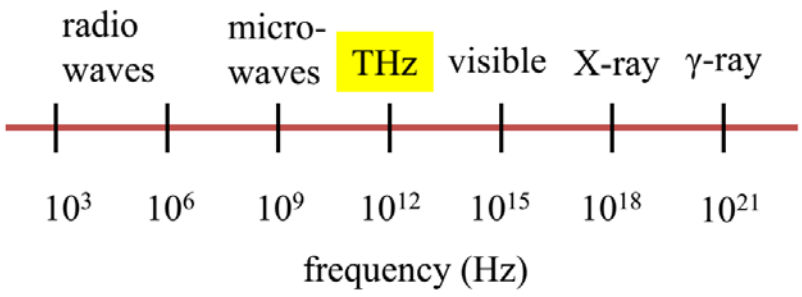

Figure 1.1 Electromagnetic spectrum.

The THz spectrum is one of the least explored regions in electromagnetic radiation due to technological difficulties in generating, detecting and controlling its radiation [1]. Assisted by the development of femtosecond lasers since the 1980s, broadband THz generation and detection has become more accessible in the laboratory. In parallel, advances in high-frequency vacuum electronics have pushed its generation spectrum from gigahertz (GHz) to sub-THz frequencies. In addition to THz sources and detectors, various materials have been developed for THz filters, wave plates and polarizers [2]. These new developments have begun to close the so-called “THz gap”, and THz technologies are now being widely applied to study various phenomena in physical, chemical and biological systems [3].

Many materials exhibit unique properties at THz frequencies. Water is strongly absorptive at THz frequencies because THz waves can excite rotational modes in water molecules [4]. Metals are highly reflective at THz frequencies due to their high electrical conductivities. However, dielectric materials such as paper, plastics, clothes, wood, and ceramics, usually opaque at optical wavelengths, are transparent at THz frequencies. These properties are useful for practical THz imaging and sensing. For example, as many packaging materials are made of plastics, THz imaging can be readily applied for nondestructive testing to inspect sealed packages where hydrated and metallic materials can be separated from others [5].

Many natural phenomena also occur at the THz frequency range. For simple molecules such as carbon monoxide, the transition frequency between its rotational levels lies at THz frequencies [6]. For much bigger and complicated molecules such as proteins, the timescales of their vibrational motions are on the order of picoseconds, corresponding to THz periods [7]. THz radiation is also applied to study wave packet dynamics of Rydberg atoms [8] as the binding energy of their electrons lies in meV, corresponding to THz photon energies. Carrier dynamics in semiconductors, semiconductor nanostructures and superconductors are extensively studied with THz radiation as well [9–11].

There are various sources for continuous or pulsed THz radiation (see Appendix A.1). In general, broadband THz pulse generation requires femtosecond lasers. One common method is using optical rectification of femtosecond laser pulses in a noncentrosymmetric crystal such as zinc telluride (ZnTe) or gallium phosphide (GaP). A novel approach for broadband THz pulse generation is to ionize gas media

with ultrashort laser pulses. This method is detailed in the next section. In particular, we focus on THz generation from laser-produced plasmas in two-color laser fields.

1.2 THz generation from laser-produced plasmas

When an intense laser pulse is focused into a target (solid, liquid or gas), the atoms in the target are rapidly ionized by the driving laser field, and a plasma is formed in the focal volume. The mechanism of photoionization is discussed in detail in the next section. Typically, photoionization occurs when the laser field strength becomes compatible to the atomic Coulomb field. For example, the Coulomb field of the hydrogen atom is around 5×10^9 V/cm, corresponding to a laser intensity of $\sim 3 \times 10^{16}$ W/cm^2. This intensity is moderate and readily achievable with today's laser technology. Following photoionization, the freed electrons are accelerated by the driving laser field. Many interesting phenomena such as high harmonic and THz generation occur during this process. Also, these laser-produced plasmas are attractive sources for mid-infrared radiation, supercontinuum light, attosecond pulses and X-rays.

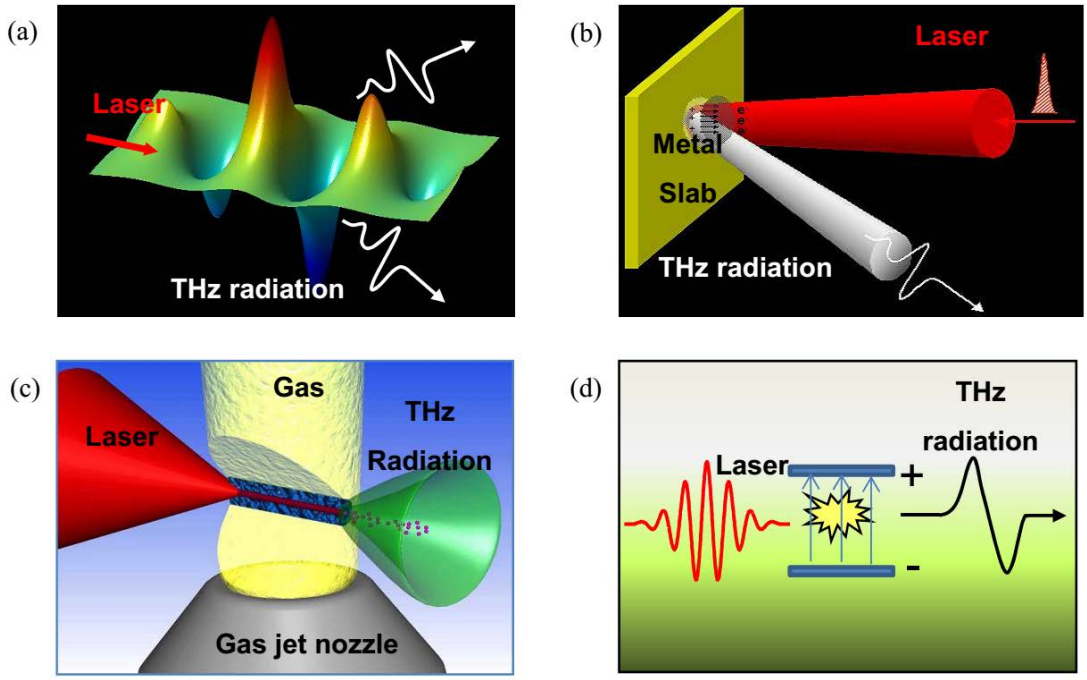

Figure 1.2 Schemes for THz generation in plasmas by (a) plasma current generation by ponderomotive forces, (b) laser-metal interaction, (c) transition radiation (courtesy of W. Leemans), and (d) static field biasing.

The first observation of THz generation from laser-produced plasma is reported by Hamster *et al*. in 1993 [12]. By focusing high-intensity laser pulses into a gas, they observed THz pulses emitted from the plasma formed at the focal spot (see Figure 1.2(a)). The mechanism was attributed to a ponderomotive force in the plasma. The ponderomotive force is a nonlinear force experienced by charged particles in an inhomogeneously oscillating electromagnetic field [13]. The force separates free electrons from ions due to their huge mass difference. This charge separation occurs within the laser envelope (sub-picoseconds), and emits electromagnetic wave corresponding to THz frequencies. Hamster *et al*. also reported THz emission from laser-irradiated solid targets [12]. They focused a *p*-polarized laser pulse on an Al-coated glass slide and observed maximum THz radiation in the direction of specular

reflection (see Figure 1.2(b)). This generation process is explained on the basis of ponderomotively-induced space charge fields on the metal surface [12].

Another method for intense THz generation is transition radiation (see Figure 1.2(c)). Transition radiation happens when a charged particle passes through a boundary between two different media. In 2003, Leemans *et al*. reported THz waves emitted from laser-accelerated electrons passing through a boundary between plasma and vacuum [14]. In their experiment, a laser pulse with peak power of 8 TW was focused into a supersonic helium gas jet inside a vacuum chamber. A dense, sub-picosecond electron bunch was produced and accelerated by laser wakefield acceleration. The energetic electron bunch emitted THz transition radiation when it crossed the boundary between plasma and vacuum.

In general, the efficiency of THz generation in plasma produced by single-color laser pulses is quite low ($<10^{-6}$ with sub-TW laser input power). This efficiency can be enhanced by adding a static electric field across the laser-produced plasma [15,16]. This was first demonstrated by Loffler *et al*. in 2000 [15]. Freed by single-color photoionization, electrons are accelerated by an external static electric field, yielding a transient plasma current and emitting a pulsed THz wave (see Figure 1.2(d)). Here, the THz output field scales with the applied static field. However, this scaling is fundamentally limited by the maximum static field applicable in air (<30 kV/cm) due to electrical breakdown.

Further enhancement can be achieved by mixing the fundamental optical pulse with its second harmonic [17–19]. This was first discovered by Cook *et al*. in 2000 [17]. Figure 1.2 shows a schematic set-up of this method. A fundamental pulse

(ω) propagates through a nonlinear crystal such as Beta-Barium borate (BBO) which creates a second harmonic pulse (2ω). These two pulses co-propagate and focus into air, which ionize air molecules at the focal spot. The resulting plasma emits a THz pulse in the forward direction.

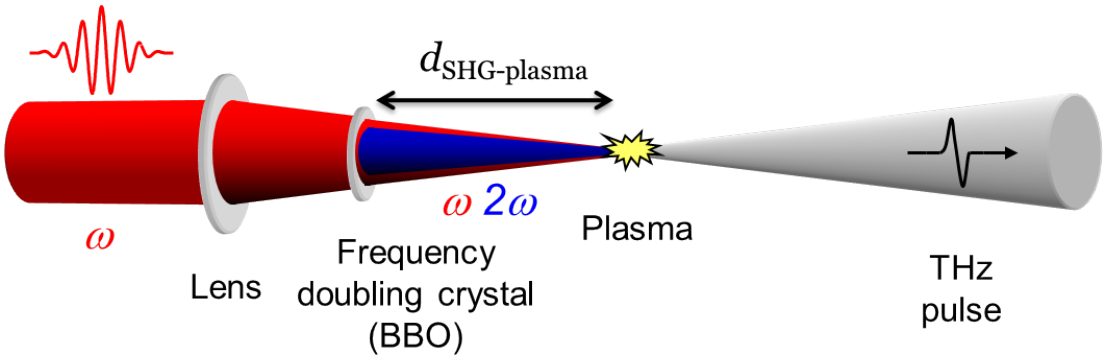

Figure 1.3 Schematic setup for THz generation from two-color laser-produced plasma.

This two-color method has two appealing features: high conversion efficiency and ultrabroad bandwidth. The conversion efficiency of this method is ~10^{-4}, two orders of magnitude higher compared to the single color case. The output THz yield is also scalable with increasing input laser energy. It has been shown that the output THz field can be as high as several MV/cm with an input laser energy of 15 mJ [20]. Another distinct feature of this THz source is its ultra-broad bandwidth [21–25]. With an input pulse duration of 10 fs, the resulting THz spectrum extends from below 1 THz up to 200 THz [25]. Unlike nonlinear crystals, a lack of phonon modes in plasma prevents THz absorption, resulting in broadband THz radiation with no spectral gap. Although this scheme does not require specific gas species, atoms with lower ionization potentials have shown to yield higher THz outputs [21].

In this two-color method, coherent control of THz radiation can be achieved by modulating the relative phase difference between ω and 2ω. In practice, the phase

difference can be tuned by changing the distance between the frequency doubling crystal ($d_{\text{SHG-plasma}}$) and the plasma (see Figure 1.3). This changes the optical path lengths for ω and 2ω due to air dispersion, and their dephasing sinusoidally modulates the THz output.

When Cook *et al*. first observed THz emission from two-color laser-produced plasma [17], they attributed the effect to four-wave mixing (rectification), a third order nonlinear optical process. This is similar to second-order optical rectification, applied to explain THz emission in nonlinear crystals (see Appendix A.1). As gases such as nitrogen, oxygen and argon are centrosymmetric under field inversion, the lowest nonlinear process allowed is the third order. Here, three photons (two photons at ω and one photon at 2ω) are mixed to produce a rectified (quasi-DC) polarization term expressed as

$$\tilde{P}(\omega+\omega-2\omega) \propto \chi^3 \left| E_\omega E_\omega E_{2\omega} \right| \cos(\theta), \tag{1.1}$$

where E_ω and $E_{2\omega}$ are the laser fields of the fundamental and second harmonic waves and θ is the relative phase between those two waves. Although this explains phase-sensitive THz generation, it has several limitations. First, the χ^3 coefficient is too small to explain the high conversion efficiency (10^{-4}) of THz radiation. Second, several experiments have shown that the minimum laser intensity required to generate THz radiation coincides with the threshold value for ionization [19]. This has led to the search for a microscopic model involving ionization and plasma creation. The next section discusses a semi-classical model which provides a microscopic mechanism for THz generation on a basis of photoionization and subsequent laser driven currents.

1.3 Semi-classical model

The interaction of an atom with an intense laser field can be fully described by solving time-dependent Schrodinger equations. However, this requires extensive computation. Instead, a semi-classical model can provide an intuitive picture for such an interaction. This was first proposed by Corkum [26] and has been successfully applied to explain electron rescattering, non-sequential ionization, high harmonic and attosecond pulse generation.

The semi-classical model consists of three steps. In the first step, an intense laser field distorts the Coulomb field in an atom, suppressing the potential barrier. The bound electron sees a lowered potential well and tunnels out through the potential barrier. This tunneling effect is purely a quantum process, as part of the electron wavepacket still remains in the bound state while the other part is freed. After this tunneling, the free electron is then accelerated by the driving laser field and oscillates along the laser polarization direction (step 2). This process is simply described by classical mechanics, where the electron is treated as a charged particle driven by an oscillating electric field. Here, the electron born before the peak of the electric field drifts away from its parent atom whereas the electron born after the peak of the electric field accelerates and collides with its parent atom, emitting high-order harmonics of the fundamental frequency (step 3).

Based on this semi-classical model, Kim *et al*. proposed a plasma current model to explain the microscopic origin of THz emission in two-color laser-induced plasma [28]. The model focuses on the directional drifting of freed electrons in an asymmetric laser field produced by two-color laser pulses. This quasi-DC current

occurs on a sub-picosecond time scale, emitting electromagnetic radiation at THz frequencies.

In this section, we discuss the plasma current model in detail with simulations. First, we consider various mechanisms in photoionization and then discuss the plasma current model in two-color laser-induced ionization.

1.3.1 Mechanisms of photoionization

Photoionization is a process where one or more electrons are ejected from atoms, molecules or ions by irradiation of photons. Typical ionization potentials for atoms are in the range of 5~24 eV, far exceeding typical optical photon energies (~2 eV). Therefore, photoionization process is a highly nonlinear process.

During the 1960s, Keldysh developed a theory to describe photoionization of a single-electron atom in an intense oscillating electric field [27]. He introduced a dimensionless parameter, which is termed as the Keldysh parameter nowadays, to characterize photoionization. In atomic units, the Keldysh parameter γ can be expressed as

$$\gamma = \sqrt{U_i / 2U_p}. \tag{1.2}$$

Here U_i is the ionization potential of the atom and U_p is the laser ponderomotive potential, the cycle average energy of an electron in the oscillating laser field. It can be expressed (in atomic units) as

$$U_p = F^2 / 4\omega^2, \tag{1.3}$$

where F is the laser field strength in atomic units and ω is the laser frequency. F can be simply obtained from the laser intensity I as $F = \sqrt{I(W/cm^2)/3.55\times10^{16}}$. In Eq.

(1.2), the Keldysh parameter can be understood as a ratio between the energy required for an electron to be freed (ionization potential) and its kinetic energy acquired within one cycle of the laser field.

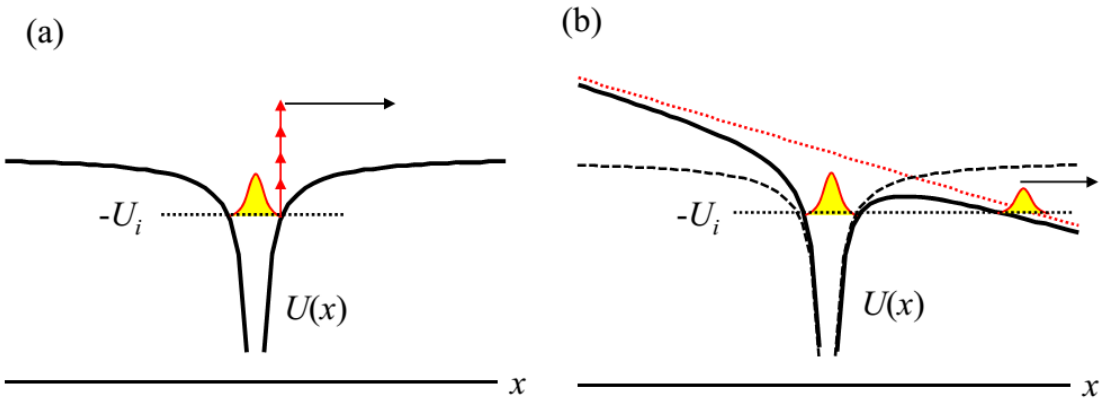

Figure 1.4 Laser induced ionization in (a) multiphoton and (b) tunneling. *U(x)* is the potential of an atom where *x* is the position. U_i is the ionization potential of the atom. The black curve represents the Coulomb barrier. In (a) multiphoton ionization, the bound electrons absorb multiple photons to be freed. In the case of tunneling ionization, the Coulomb barrier (black dashed line) is suppressed by the external electric field (red dotted line). The bound electron tunnels through the suppressed Coulomb barrier (black solid line) and becomes freed.

Another way to look at the Keldysh parameter is to express γ as a ratio of the tunneling time t_{tu}, the time required for an electron to tunnel out the Coulomb barrier, to the laser period T_0,

$$\gamma = 2t_{tu} / T_0. \tag{1.4}$$

Here we present a simple derivation for the above expression. The work *W* done by the laser field *F* to a bound electron in order to cross a barrier width Δl is $W = F\Delta l$ (e = 1). This is equivalent to the ionization potential energy, $U_p = F\Delta l$. In parallel, the electron acquire a kinetic energy of $U_p = \frac{1}{2}v^2$. Then the tunneling time is given by $t_{tu} = \Delta l / v = \sqrt{U_p} / (2F)$. By putting this back into Eq. (1.4), one can retrieve the original definition in Eq. (1.3).

For $\gamma \gg 1$, the ionization potential is much higher than the ponderomotive potential (from Eq. (1.2)), and the tunneling time is much longer than the laser period (from Eq. (1.4)). In this case, the bound electron needs to acquire several photons to be excited to the continuum and freed. This ionization mechanism is called multiphoton ionization. Here the rate of multiphoton ionization *w* can be calculated as $w = \sigma_n I^n$, where *n* is the minimum number of photons required to surpass the ionization potential (see Figure 1.4(a)) and σ_n is the generalized cross section for *n* photon absorption. This multiphoton ionization process usually happens when the laser intensity is below ~10^{12} W/cm^2 at Ti:sapphire laser wavelengths (800 nm).

For $\gamma < 1$, the ionization potential is lower than the ponderomotive potential, and the tunneling time is much shorter than the laser period. This indicates that tunneling ionization occurs within a fraction of the laser field in which the oscillating field can be assumed to be static. In this tunneling ionization regime, the Coulomb barrier is instantaneously suppressed by the laser electric field, allowing the bound electrons to tunnel out from the atom (see Figure 1.4 (b)). Typically, tunneling ionization occurs when the laser intensity approaches 10^{13} W/cm^2 and becomes dominant at >10^{14} W/cm^2 at 800 nm. In practice, the tunneling ionization rate can be calculated from an ADK (Ammosov-Delone-Krainov) model [28], expressed as

$$w(t) = 4w_a \left(\frac{E_a}{|E_L(t)|} \right) \exp\left(-\frac{2}{3}\frac{E_a}{|E_L(t)|}\right), \tag{1.5}$$

where w_a is the atomic frequency, E_a is the atomic field and $E_L(t)$ is the instantaneous electric field at time *t*. For a hydrogen atom, E_a = 5.14 × 10^9 V/cm and ω_a = 4.134 × 10^{16} s^{-1}.

1.3.2 Plasma current model

Two-color laser fields composed of the fundamental (ω) and its second harmonics waves (2ω) can be expressed as

$$E_L(t) = E_\omega \cos(\omega t) + E_{2\omega}\cos(2\omega t + \theta), \tag{1.6}$$

where E_ω and $E_{2\omega}$ denote the amplitudes of the fundamental and second harmonic waves and θ is the relative phase between two fields. For example, the combined fields for $\theta = 0$ and $\theta = \pi/2$ with ratio $E_{2\omega}/E_\omega = 0.32$ are plotted (dotted lines) in Figure 1.5. At laser intensities around $10^{14} \sim 10^{15}$ W/cm^2, the peak laser fields are compatible to the internal Coulomb field experienced by the valence electrons in atoms and molecules. These strong fields allow the bound electrons to tunnel out from the atoms and molecules. For hydrogen-like atoms, the tunneling ionization rate $w(t)$ can be calculated by Eq. (1.5). Then the electron density $N_e(t)$ produced between t and $t + dt$ is obtained from the product of the instantaneous neutral gas density $N_g(t)$ and the ionization rate $w(t)$,

$$dN_e(t) = w(t)[N_g - N_e(t)]dt \approx N_g w(t)\,dt, \tag{1.7}$$

assuming that $N_e(t) \ll N_g$, which is the case in the intensity of our interest. The red curves in Figure 1.5 indicate that tunneling ionization occurs around the peaks of the laser field. Once an electron is born at $t = t'$, it is accelerated by the external laser-field with a velocity of

$$v(t,t') = -(\frac{e}{m_e})\int_{t'}^{t} E_L(t)\,dt\,. \tag{1.8}$$

Here we assume the initial velocity is zero. The electrons liberated at different times will acquire different drift velocities, which can be expressed as

$$v_d(t') = (e/2m\omega)(2E_1 \sin(\omega t') + E_2 \sin(2\omega t' + \theta)), \quad (1.9)$$

where *e* and *m* are the electron charge and mass respectively. The drift velocities for $\theta = 0$ and $\theta = \pi/2$ are plotted in Figure 1.5 (solid blue lines). For the electrons born before the peak, they acquire a negative velocity, whereas the electrons born after the peak acquire a positive velocity. The acceleration of these electrons results in a plasma current. Here, the current density can be expressed as,

$$J(t) = \int_{t_0}^{t} ev\left(t, t'\right) N_e(t')dt', \quad (1.10)$$

where $N_e\left(t'\right)dt'$ is the density of electrons liberated by the laser field in an interval between t' and $t + dt'$. The radiated THz field is then proportional to the derivative of the current density as $E_{THz} \propto \frac{dJ(t)}{dt}$. In the case of $\theta = 0$, the electron density about the peak is symmetric (see Figure 1.5(a)), but the drift velocity is anti-symmetric. The product, shown in the gray area of Figure 1.5(a), yields zero directional current. In the case of $\theta = \pi/2$, the electron density peaks when the drift velocity is nonzero, due to the asymmetry of electric field around the peak. The gray area in Figure 1.5(b) indicates that more electrons travel in the negative direction, resulting in a directional current. This directional current surge produces THz radiation in the far field.

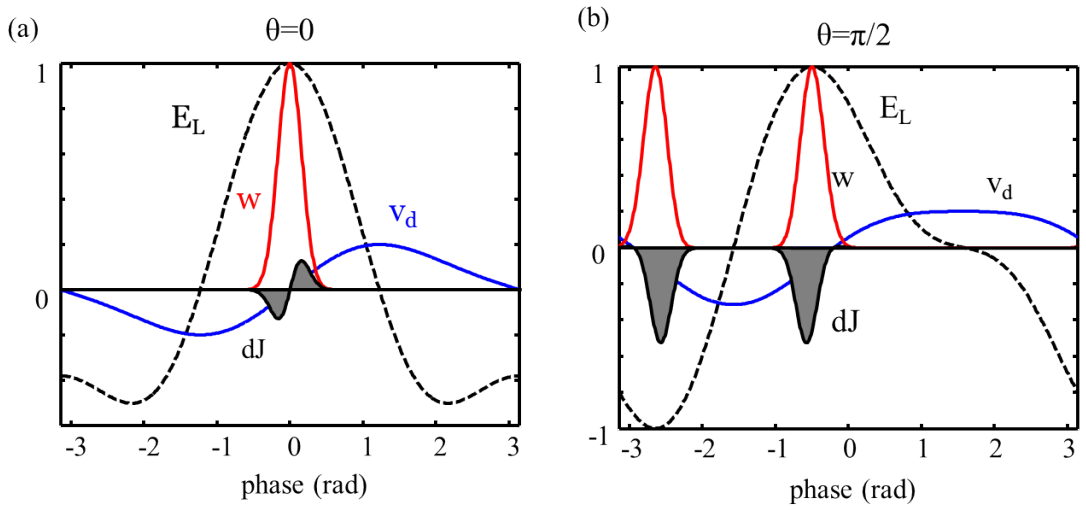

Figure 1.5 Drift velocity (blue curves) of freed electrons in a two-color field (dotted lines) for two different relative phases (a) θ=0 and (b) θ=π/2. Time-dependent ionization rates are shown in red solid curves. The gray areas indicate the product of electron density and drift velocity.

In the plasma current model, THz radiation can be simulated for typical experimental conditions. Here, the electric field of the fundamental (ω) and second harmonics wave (2ω) can be expressed as

$$E_L(t) = E_\omega(t)\cos(wt) + E_{2\omega}(t)\cos(2wt+\theta), \tag{1.11}$$

where, $E_\omega(t)$ and $E_{2\omega}(t)$ are assumed to be Gaussian envelopes with peak laser intensities of $I_1 = 10^{14}$ W/cm^2 at $\lambda_w = 800$ nm and $I_2 = 10^{13}$ W/cm^2 at $\lambda_{2w} = 400$ nm with the same pulse duration of 30 fs. The target gas is nitrogen with an initial gas density of $N_g = 2.4\times10^{19}$cm^{-3}. The relativistic and magnetic field effects are negligible at the laser intensities considered here and therefore ignored. Electron-ion collisions are not considered in the simulation since the expected collision time (~1 ps) under our condition is much longer than the laser pulse duration. The Coulomb field interaction between electrons and their parent ions is excluded for simplicity. The time window of the simulation is 90 fs with a time step of 0.01 fs.

Figure 1.6 shows the evolution of ionization (red) and electron density (black) as a function of time for two different relative phases (a) $\theta = 0$ and (b) $\theta = \pi / 2$. As discussed earlier, tunneling ionization mostly occurs around the peaks of the oscillating laser field, and it is sensitive to the relative phase. Therefore the occurrence of ionization for these two cases is different: one ionization event per cycle for $\theta = 0$ while two for $\theta = \pi / 2$. Note that the electron density increases in a step-wise manner because of this instantaneous ionization.

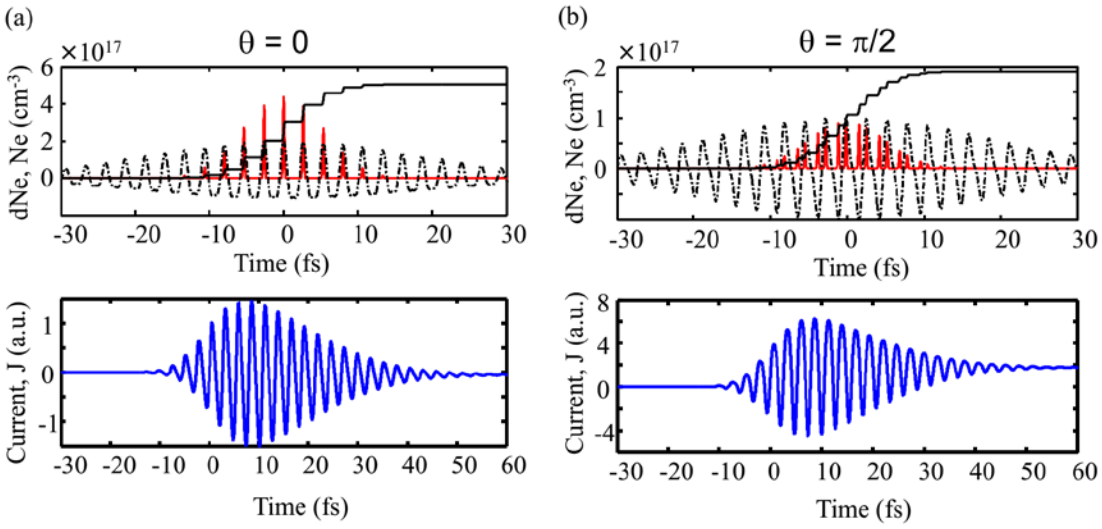

Figure 1.6 Electric field (dotted line), ionization rate (red curve), free electron density (black curve) and current density (blue curve) as a function of time with (a) $\theta = 0$ and (b) $\theta = \pi/2$.

Taking ionization and subsequent electron motion into account, we can simulate its time-varying electron density. As shown in Figure 1.6, a directional current occurs only with (b) $\theta = \pi / 2$. Here, the rise time of the current determines its radiation bandwidth. As the current surge occurs much faster than the laser pulse duration, broadband radiation is expected. The radiation spectrum is calculated by Fourier transformation and plotted in Figure 1.7(a) for three different cases ($\theta = 0$, $\theta = \pi / 2$ and ω alone). With no second harmonic, there is no transverse, directional

current surge. A quasi-DC current appears with second harmonic mixing, and its magnitude greatly enhances with $\theta = \pi / 2$. Another interesting feature is an anti-correlation between THz and third harmonic radiation. With $\theta = \pi / 2$, THz is enhanced whereas the third harmonic is suppressed, and vice versa with $\theta = 0$. Figure 1.7(b) confirms this trend by showing simulated THz and third harmonics yields as a function of the relative phase θ. It is shown that they are both sensitive to θ and anticorrelated with each other.

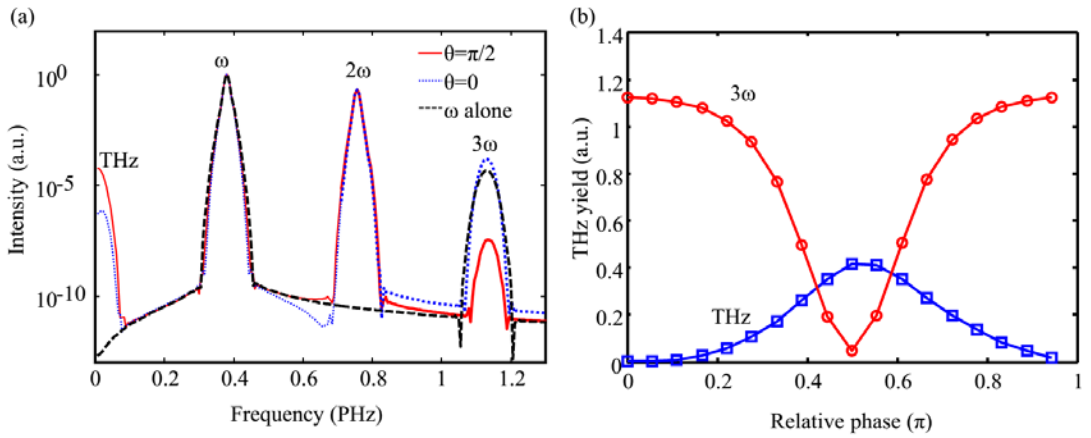

Figure 1.7 (a) Radiation spectra for single color only (black curve), two color with $\theta = 0$ (blue curve) and with $\theta = \pi/2$ (red curve). (b) THz (blue curve) and third harmonic yield (red curve) as a function of relative phase θ.

1.4 About the thesis

The main theme of this dissertation is to investigate THz emission from two-color laser-produced plasmas, revealing its mechanisms at both microscopic and macroscopic levels. In this chapter, we have reviewed various schemes for THz generation in laser-produced plasmas including the two-color laser based method. In general, plasma-based methods have lower conversion efficiencies compared to solid-state-based methods. However, because of their damage-free property in plasmas, the output THz power, in principle, is scalable with input laser power. In particular, the

two-color laser method yields extremely broadband THz radiation compared to solid-state methods.

In Chapter 2, we discuss simultaneous measurements of near-field plasma currents and far-field THz radiation, all calibrated by directly-measured relative phases between two-color laser fields. This study is of great importance in verifying the plasma current model, as discussed in this Chapter.

In Chapter 3, we study THz emission from aligned air molecules in two-color laser fields. It is known that ionization of molecules strongly depends on their orientation with respect to the input laser field. This can greatly affect THz generation from air molecules ionized by intense laser fields. Our result shows that air molecules aligned parallel with two-color fields yield more THz radiation.

In Chapter 4, we switch our attention from a microscopic description to its macroscopic one for THz generation. We discuss our work on phase-matched THz generation, which is crucial to achieve high power THz outputs.

In Chapter 5, we discuss the polarization of THz output radiation in two-color photoionization, addressing why the resulting THz polarization is elliptical. We show that this ellipticity arises from two combined effects—successive polarization rotation of local THz plasma sources, caused by laser phase and polarization modulations, and the velocity mismatch between laser and THz pulses.

Chapter 2 : Phase Dependence of THz Emission from Two-Color Laser-Induced Plasma

2.1 Introduction

As discussed in the previous chapter, many experiments have confirmed that the THz output amplitude can be coherently controlled by modulating the relative phase θ between the fundamental and its second harmonic fields [19,29,30]. Two models have been presented to explain this phase dependence: four-wave mixing [29] and plasma current model [21,30]. The predictions by these two models contradict each other, where maximal THz generation is predicted at $\theta = 0$ (or π) in four-wave mixing but at $\theta = \pi/2$ (or $3\pi/2$) in the plasma current model.

Recently, Zhang *et al*. reported $\theta \approx 0.83\pi$ for optimum THz emission by observing concurrent high order harmonics [31]. Their observation was explained by a plasma current model including electron-ion scattering. This involves the electron wavepacket scattered by its parent ion, where the Coulomb field of the ion alters the momentum of the electron wavepacket and its subsequent motion. This momentum transfer depends on the field strength between atomic core and laser, which can shift the optimal phase for THz radiation.

To clarify such a microscopic origin for THz generation, a direct measurement of the optimal relative phase for THz radiation is necessary. In most experiments involving two-color laser pulses, the relative phase between two-color fields is not measured directly. Rather, it is indirectly inferred from models. To avoid this ambiguity, we apply an interference method to directly measure the relative phase θ at the laser focus where THz radiation originates. Simultaneously we monitor output

THz yields with varying θ. These measurements are conducted under various conditions including different gas species, laser intensities, and two-color amplitude ratios in order to verify the optimum relative phase for THz generation.

2.2 Experimental set-up

In the experiment, THz pulses are generated with 40 fs, 1 kHz, 800 nm laser pulses in a backfilled vacuum chamber at ~40 mTorr pressures. First, second harmonics (400 nm) are produced from a thin BBO (BaB_2O_4) (see Figure 2.1). The relative phase between the second-harmonic and the fundamental fields is controlled with a pair of wedged fused silica where the insertion of one of the wedges changes the relative phase between two beams without changing their beam directions. Group-velocity dispersion experienced in the fused silica is compensated by a calcite birefringent crystal. Finally, to obtain two-color fields with co-linear polarization, a zero-order waveplate is inserted, which rotates the fundamental and second-harmonic fields by $90°$ and $180°$, respectively. An off-axis parabolic mirror is used to focus the fundamental and second harmonics into a backfilled gas (Ar, He, O_2, or N_2) to create a gaseous plasma. THz pulses emitted from the plasma are collected and focused by a pair of off-axis parabolic mirrors for detection. The center of the first collecting parabolic mirror has a hole with diameter of 0.5 mm to transmit two-color laser pulses for their relative phase measurements. The principle of relative phase measurements is detailed in the next section. The emitted THz waves are detected via electro-optic sampling (EOS) using with a 1 mm thick ZnTe [110] crystal, which detects THz radiation from 0.1 to 3 THz. A complementary measurement conducted

with a pyroelectric detector capable of covering 1~100 THz coincides with the EOS measurement.

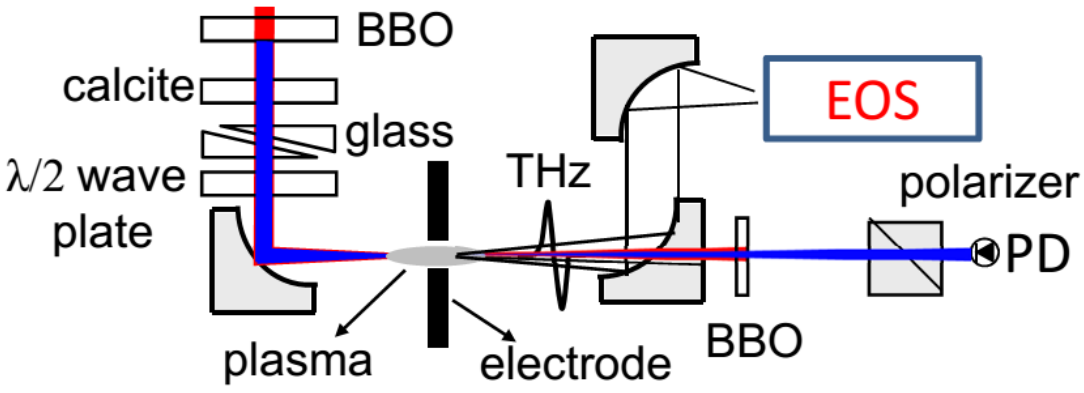

Figure 2.1 Schematic set-up of experiment.

The photocurrent produced by two-color photoionization is detected by an electrode of ~1 mm^2 cross-sectional area placed at ~1 mm away from the focal point. The current is triggered by charged particles striking the electrode surface and analyzed with an oscilloscope. Figure 2.2(a) shows sample photocurrent signals measured as a function of background pressure. The signal peaks around 1 Torr and then diminishes quickly with increasing pressure. This trend confirms that the detected signal is due to charged particles not radiation. The strongly damped signal at higher pressures can be understood as scattering and absorption of charged particles by high-density gas molecules. At extremely low pressures (< 1 Torr), the signal also drops because the background gas density approaches zero. The maximum signal appears around 1 Torr as a result of these two counteracting effects.

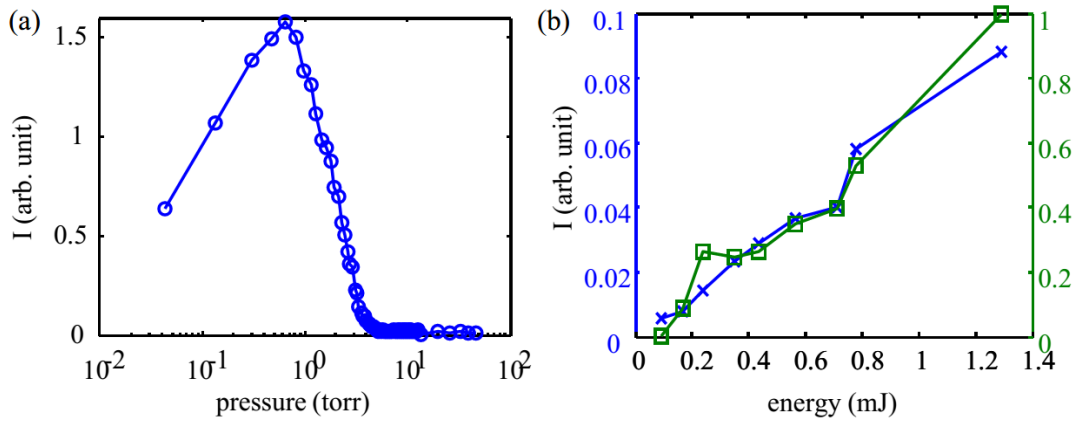

Figure 2.2 (a) Measured photocurrent with increasing backfilled pressure. (b) THz (green curve with squares) and photocurrent (blue curve with cross) yields versus input laser energy.

2.3 Interferometric measurement of relative phase

An interferometric measurement of the relative phase between a fundamental (ω) and its second harmonic (2ω) pulses is first reported by Chudinov *et al*. [32]. This method was previously applied to study phase-dependent tunneling ionization [33]. In principle, the phase difference between ω and 2ω is measured by observing the interference between the original 2ω and a new 2ω produced by ω in another second harmonic crystal [32,34]. Figure 2.3 shows a schematic for such measurements. First, collinearly-polarized ω and 2ω pulses with an unknown relative phase are directed to a BBO crystal. When the ω pulse propagates through the BBO crystal, it generates a "new" 2ω pulse. Since second harmonic generation (SHG) is phase-locked, the relative phase between ω and 2ω is transferred to a relative phase between the "new" and "old" 2ω. Here the BBO crystal needs to be azimuthally rotated away from its phase matching angle such that the "old" 2ω beam has a component parallel to the "new" 2ω beam, and interference can occur along the extraordinary axis (*e*-axis) of BBO. Then a filter transmitting 2ω is used to block the fundamental ω beam,

followed by a polarizer used to transmit the 2ω beams polarized along the e-axis. The filter and polarizer combination does not change the relative phase because the material dispersion experienced by the "new" and "old" 2ω is identical. Finally, the interference between "new" and "old" 2ω is measured by a GaP photodiode. The resulting interference signal varies with θ, where the maximum and minimum signal occurs $\theta = 0$ and $\theta = \pi$, respectively (see Figure 2.3).

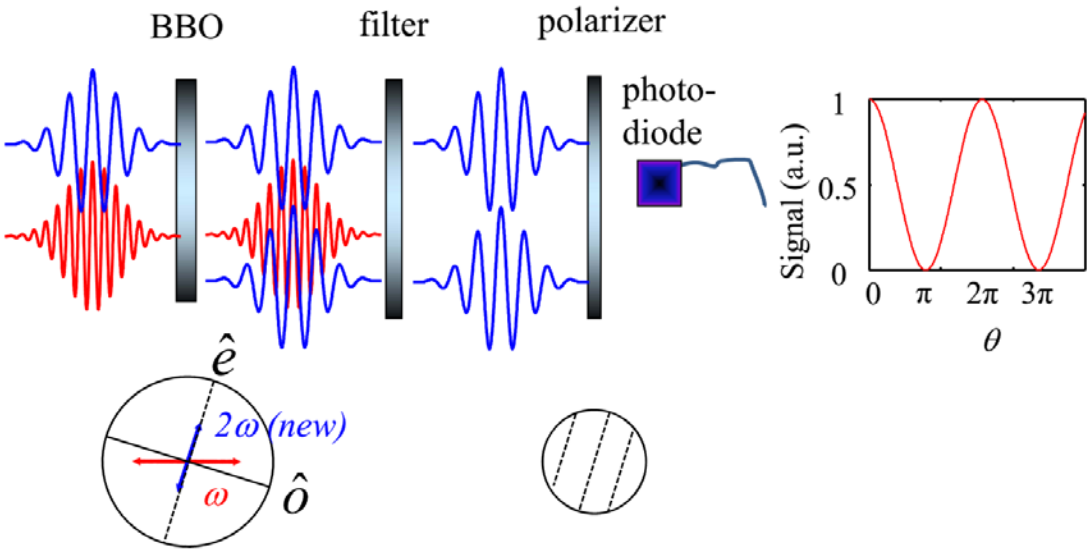

Figure 2.3 Scheme for interferometric measurements of the relative phase between ω and 2ω.

Since our interest is to measure the relative phase at the focal point where THz pulses are emitted, several effects need to be taken into account: the dispersion of gas medium, relative phase after the second harmonic crystal, and Gouy phase shift induced by focusing. First, our measurement is carried out in a vacuum chamber with backfill pressures lower than 1 Torr. This is to minimize self-phase modulation and spectral blue-shifting due to high intensity focusing in the focal volume. Such effects can be ignored at low gas pressures. In our experiment, we observe that the interference signal disappears at pressures beyond 100 Torr. This indicates that low

pressures are necessary for accurate measurements of the relative phase. Such a condition also excludes consideration of gas dispersion. At atmospheric pressure, the relative phase between ω and 2ω changes by π over a ~2.8 cm distance due to dispersion in air. By measuring the relative phase at 10^{-3} atmospheric pressure (~0.76 Torr), gas dispersion can be ignored for a propagation length of tens of cm, avoiding the ambiguity in determining the focal point.

It is notable that the relative phase between ω and 2ω is not zero but $\theta = \pi / 2$ in the second harmonic generation (SHG) process. According to [35] (see Eq. 2.2.9), the second harmonic field during its generation process can be expressed as

$$\tilde{E}_{2\omega}(z) = \frac{2id_{eff}(2\omega)^2 \tilde{E}_{\omega}^2}{k_{2\omega}c^2}\left(\frac{e^{i\Delta kz}-1}{i\Delta k}\right), \tag{2.1}$$

where d_{eff} is the nonlinear coefficient, $k_{2\omega}$ is the wave vector for the second harmonic and Δk is the phase-mismatching term. For phase-matched second harmonic generation, such as in a BBO crystal, $\Delta k = 0$ and $\left(\frac{e^{i\Delta kz}-1}{i\Delta k}\right) \sim z$. Therefore, $\tilde{E}_{2\omega}(z)$ is approximated as

$$\tilde{E}_{2\omega}(z) \propto id_{eff}\tilde{E}_{\omega}^2 z. \tag{2.2}$$

In the case of BBO, d_{eff} is real. Therefore, the phase difference between ω and 2ω is $\theta = \pi / 2$, constant throughout their propagation in the crystal.

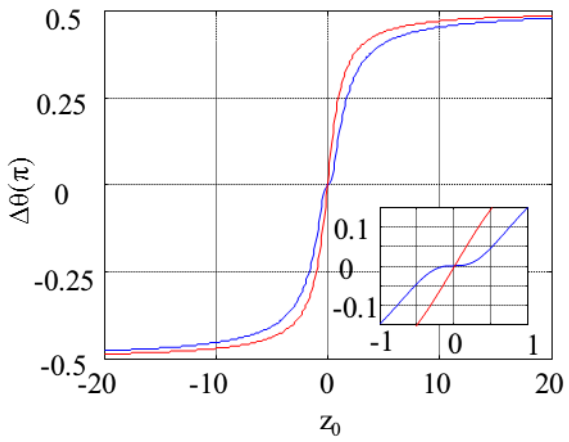

Figure 2.4 Calculation of the Gouy phase for a single color wave (red curve) and the difference of the Gouy phases for two-color waves, the fundamental and its second harmonic waves (blue curve). The lower left inset shows a close-up near the focal point.

A focused laser pulse acquires an extra phase (Gouy phase shift). Individual Gouy phase shifts for ω and 2ω along the Gaussian beam axis can be described as $\phi_{\omega,2\omega} = \tan^{-1}(z / z_{0;\omega,2\omega})$, where $z_{0;\omega,2\omega}$ is the Rayleigh length of ω and 2ω beam, respectively, and $z = 0$ defines the focal position. The relative phase difference between ω and 2ω, at the center of the beam, caused by the Gouy phase shift is

$$\Delta\phi = 2\phi_{\omega} - \phi_{2\omega} = 2\tan^{-1}(z / z_{0,\omega}) - \tan^{-1}(z / z_{0,2\omega}). \qquad (2.3)$$

The Rayleigh range can be expressed as $z_0 = \lambda / \pi\Theta^2$, where λ is the wavelength and Θ is the numerical aperture. By keeping the same Θ for both beams, we get $z_{0,2\omega} = 0.5 z_{0,\omega}$. With a Taylor expansion at $z = 0$, the relative phase shift around the focal point can be approximated to be zero from $\Delta\phi \sim 2z / z_{0,\omega} - z / z_{0,2\omega} \sim 0$. A simple calculation shows that it is nearly constant for almost one Rayleigh length around the focus (see the inset in Figure 2.4). At the far field $z = \infty$, the relative phase is $\Delta\phi = 2(\pi / 2) - \pi / 2 = \pi / 2$. This Gouy phase shift effect was confirmed in our

experiment by measuring the relative phase before and after focusing, with a change of phase equal to π. In the experiment, the second BBO is placed ~10 times the Rayleigh length away from the focal point, ensuring that the relative phase is almost $\pi/2$.

The combined effects of second harmonic generation (π/2) and Gouy phase shifting (π/2) gives rise to a relative phase of π. Therefore, the constructive (destructive) interference signal detected by the photodiode should be interpreted as θ = π (0) at the focal point.

An additional effect to be considered is the plasma dispersion around the focal point. Here, the phase slippage between ω and 2ω is given by $\delta\theta \approx (3\pi/4)(l/\lambda)(N_e/N_c)$, where N_e is the plasma density and $N_c \sim 2\times10^{21}\,\mathrm{cm}^{-3}$ is the critical plasma density at 800 nm. Under our experimental condition, the neutral density is $\sim 2\times10^{16}\,\mathrm{cm}^{-3}$ and N_e is estimated to be ~ $1.4\times10^{13}\,\mathrm{cm}^{-3}$ at a laser intensity of $8.3\times10^{13}\,\mathrm{W/cm}^2$. With a plasma length l ~2 mm, measured from side imaging of fluorescence emission, we estimate the phase slippage $\delta\theta$ to be 10^{-6} rad, which is small enough to be neglected.

We note that a similar interferometric method was previously applied to measure the relative phase [36]. In their measurement, however, the relative phase was measured at the focus. This requires strongly attenuated laser intensities at the focal point, which does not represent the exact experimental condition. Moreover, their phase measurement is carried out at atmospheric pressure, which provides unwanted phase slippage as high as 0.1π for a 2 mm long plasma (<1% ionization), adding an extra uncertainty in measuring θ.

2.4 Relative phase measurement with interferometric and photocurrent detection (method I)

Figure 2.5 summarizes our measurements of THz radiation, interferometric 2ω, and plasma current as a function of the relative phase θ. The results are obtained by focusing 1.2 mJ, 40 fs laser pulses at a 2ω-to-ω intensity ratio of 10% in a backfilled (50 mTorr air) vacuum chamber (see Figure 2.1). Figure 2.5(a) shows THz outputs modulated by variable relative phases. The inset shows a THz waveform taken at $\theta = \pi/2$. Figure 2.5(b) shows the interference signal of 2ω (see Section 2.3) which is used to calibrate the relative phase θ. It shows that the THz output is maximized at $\theta = \pi/2$ and minimized at $\theta = 0$. Figure 2.5(c) shows the measured photocurrent as a function of θ. The current signal shows a sinusoidal modulation peaked at $\theta = -\pi/2, \pi/2, 3\pi/2$ and $5\pi/2$, coinciding with the THz modulation shown in (a). Figure 2.2(b) shows the variations of current and THz signals as a function of input laser energy. It shows that both outputs increase almost linearly with increasing laser energy. This strong correlation confirms the plasma current as a source for far field THz radiation. We note that our photocurrent detection does not measure photoelectron energies. For such a measurement, energy-resolved electron spectroscopy can be performed but it requires much lower gas densities (pressures lower than 10^{-4} Torr) [37]. However, such a low density would yield little or no detectable THz emission, making it difficult to confirm the correlation between THz and photoelectron generation.

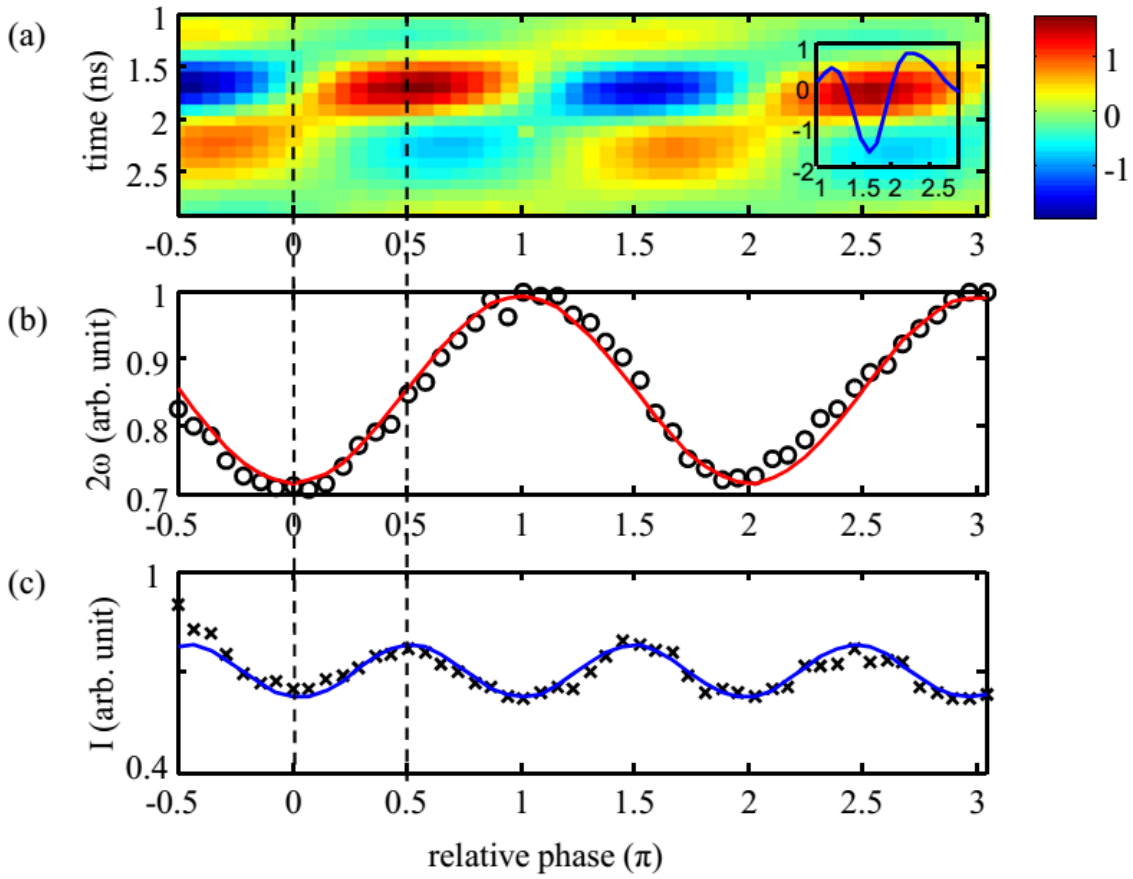

Figure 2.5 Measured (a) time-domain THz, (b) 2ω interference, and (c) photocurrent signals. The inset in (a) shows a typical THz waveform obtained at a relative phase of $\pi/2$. The relative phase between ω and 2ω is determined by the 2ω interference measurement. The blue and red curves are fitting curves. The vertical dotted lines indicate minimal and maximal THz radiation.

We have conducted the measurement with varying laser intensities, gas species and the ratio between the fundamental and second harmonic field amplitudes. The results are summarized in Figure 2.6. First, Figure 2.6(a) shows measured optimum phases and THz yields with input laser energies ranging from 167 μJ to 1.29 mJ, with corresponding intensities of 1.1×10^{14} W/cm^2 to 8×10^{14} W/cm^2. Here, the Keldysh parameter ranges from 1.1 to 0.4, covering both multi-photon and tunneling ionization regimes (see Chapter 1). The result shows that the THz output yields maximally at $\theta = \pi/2$ (or $3\pi/2$), regardless of input intensities. Also the THz outputs

increase with input energies as expected. Note that the lowest detectable THz signal appears with an input energy of 167 μJ, similar to 160 μJ reported in [19]. Figure 2.6 (b) shows the optimum phases and resulting THz yields for different gas targets including helium ($I_p = 23$ eV), argon ($I_p = 15.76$ eV), nitrogen ($I_p = 23$ eV), and oxygen ($I_p = 12$ eV), at a laser intensity of 8×10^{14} W/cm^2, with 0.5 Torr pressure. The corresponding Keldysh parameter ranges from 0.34 to 0.5. The result shows that the THz yield maximizes at $\theta = \pi/2$ (or $3\pi/2$), regardless of gas species. Figure 2.6(c) shows the measured optimum phases and THz yields for different ratios of $E_{2\omega} / E_{\omega}$. Here, the ratio is adjusted by detuning the first BBO crystal from the phase-matching angle. The result shows the optimal phase of $\pi/2$, regardless of the ratio, which also supports the plasma current model.

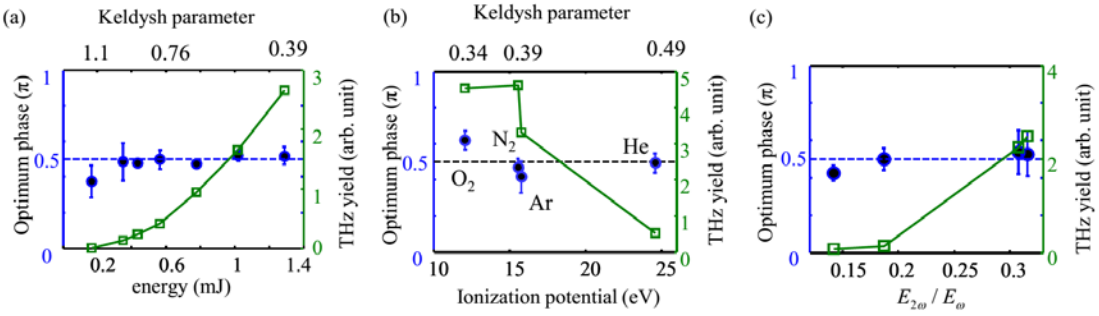

Figure 2.6 Measured THz yields (green squares) and optimal phases (blue circles) for THz emission under various conditions including different (a) laser energies , (b) gas species , and (c) amplitude ratios of the second harmonic to the fundamental fields. The dashed lines) indicate $\theta = \pi/2$.

2.5 Relative phase measurement with pressure scanning (method II)

As a secondary method to measure the optimal relative phase, we have measured THz output yields with varying backfilled pressures. This scheme is shown in Figure 2.7. The experimental setup is similar to that described in Section 2.2. One difference is that instead of biprisms low-pressure air is used as a dispersive material

to control the relative phase θ between ω and 2ω, which is given by $\theta = 2\omega(n_\omega - n_{2\omega})l/c + \theta_0$. Here $n_{\omega,2\omega}$ is the refractive index of air at ω and 2ω frequency [38] respectively, l = 23.8 cm is the distance between the BBO crystal and the focal point (see Section 2.3). θ_0 includes the phase shifts induced by the BBO (π/2), dual waveplate (0), transformation from plane to curved wavefront (π/2), mirror reflection (π), and Gouy phase shift (-π/2), which leads to $\theta_0 = 3\pi/2$. Here, we assume that the refractive index scales linearly with background gas pressure P, as in $n(P) = n_0 P[torr]/760[torr]$, where n_0 is the refractive index at 1 atm. By changing the pressure inside the chamber, one can effectively control the relative phase θ at the focal point as $\theta(P) - \theta_0 = \alpha P[torr]/760[torr]$, where $\alpha = 2\omega(n_\omega - n_{2\omega})l/c$. At low pressures (<1 Torr), the relative phase is close to $\theta_0 = 3\pi/2$ at the focal point. This reference can be used to determine the optimal relative phase with pressure scanning.

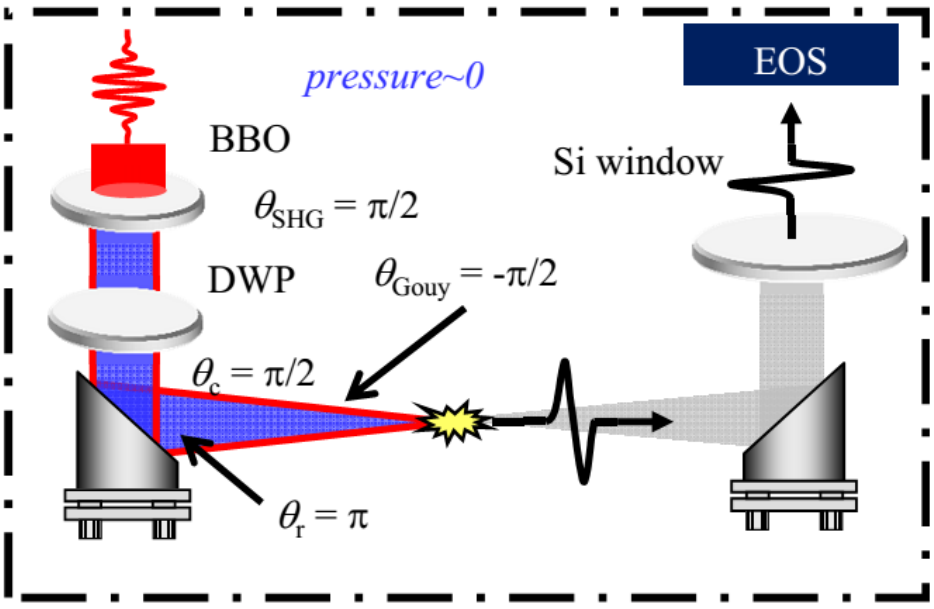

Figure 2.7 Schematic set-up in a vacuum chamber designed to determine the optimal relative phase between 800 nm and 400 nm pulses at the focus.

Figure 2.8 (a) shows a time-domain THz field measured by EOS at pressures of 0.05 to 500 Torr. The inset shows a THz waveform obtained at 330 Torr (dotted line). The corresponding THz yield ($E_{\mathrm{THz}}{}^2$) is plotted in Figure 2.8(b) (red squares). The black curve is a fitting curve obtained with $\sin^2\theta(P)$. The extrapolated curve at near-zero pressure predicts maximal THz emission. Note that the actual signal, however, approaches zero at low pressures simply because of lack of gas molecules to be ionized. The extrapolation confirms that maximal THz emission happens at $3\pi/2$ (or $\pi/2$), which is in accordance with the result obtained with the interferometric method.

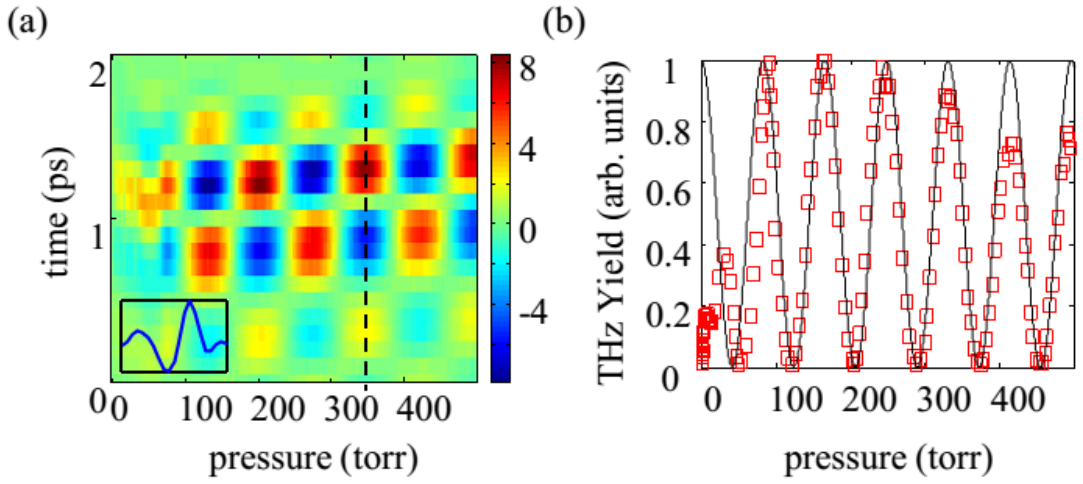

Figure 2.8 (a) Measured time-domain THz fields as a function of background gas pressure. The inset in (a) shows a THz waveform obtained at 330 Torr (dotted line). (b) Measured THz yields (red squares) with a fitting curve of a sine-squared function (black curve).

2.6 Discussion

As discussed in Section 2.1, the semi-classical plasma current model predicts an optimal relative phase of $\pi/2$. In the model, tunneling ionization is assumed, and this remains valid in the Keldysh range (0.4 ~ 1.1) we have explored herein. However, for $\gamma \gg 1$, where the laser intensity is much lower than 10^{13} w/cm^2, the

expected THz yield is several orders of magnitude lower, and therefore it is hardly detectable. In general, nonlinear polarization P_{NL} for THz emission can be expressed from contributions from both bound (P_{FWM}) and free electrons (P_J), $P_{NL} = P_{FWM} + P_J$, where $P_{FWM} = 12\epsilon_0 \chi^{(3)} \left| E_\omega E_\omega E_{2\omega} \right| \cos\theta$, $P_J = iJ / \omega_T$ and $\chi^{(3)}$ of air is $1.27 \times 10^{-27} \mathrm{m}^2/\mathrm{V}^2$ [35]. At a laser intensity of 10^{14} W/cm^2, the ratio P_{FWM} / P_J is estimated to be 7×10^{-3}. This indicates that the contribution from four-wave mixing is negligible for THz generation at the laser intensity of our interest, especially at low THz frequencies [39,40]. However, at higher THz frequencies (mid-infrareds) , four-wave mixing contributes significantly [41,42].

In our experiment, we observe a constant optimal phase θ for a broad range of γ. This contradicts with the prediction by Zhang *et al.* [31]. This observation indicates that electron scattering by an ion core does not significant affects the overall plasma current. Here, we estimate the contribution from electron scattering. When a bound electron tunnels out from its atomic Coulomb potential, its wavepacket has a radial distribution of $e^{-r/r_\perp}$, where $r_\perp$ is the characteristic radius of atom. For argon, the characteristic radius is $r_\perp = \sqrt{2} \times 0.19$ nm. Once liberated from the atom core, the electron wavepacket spreads with time due to the uncertainty principle. Its width can be calculated as $r_\perp^{'}(t) = \sqrt{(v_\perp t)^2 + {r_\perp}^2}$, where $v_\perp = \hbar / m r_\perp$ is the transverse velocity of the wavepacket. For argon, after one laser cycle (2.67 fs), the radius of the wavepacket becomes ~7.2 nm. From these, the probability for a hard collision is estimated to be $(0.27/7.2)^2 \sim 1.4\times10^{-3}$, far too small to alter the plasma current.

Therefore, we conclude that electron scattering by ion cores plays little role in determining the plasma current and affecting THz radiation.

2.7 Conclusion

In conclusion, we confirm that the optimal relative phase for THz generation is ~$\pi/2$, not significantly affected by gas species, laser intensities, and intensity ratios between two-color laser fields. These results are in accordance with the semi-classical plasma current model discussed in Chapter 1. We also observe a strong correlation between microscopic photocurrents and resulting THz radiation. This measurement also verifies directional current transients as a microscopic source for far-field THz radiation in two-color laser-produced plasmas. In addition, our approach of measuring the relative phase between fundamental and second harmonic fields can be readily applied to other two-color coherent control systems such as photocurrent production in semiconductors [43] and on metal surfaces [44], as well as high-harmonic generation [45] and dissociation of molecules [46,47] in intense two-color laser fields.

Chapter 3 : THz Generation from Pre-Aligned Molecules

3.1 Introduction

In this chapter, we investigate how THz radiation is influenced by molecular alignment during tunneling ionization. Recent studies show that molecular ionization greatly depends on the angle between the incident electric field and the molecular axis [48,49]. This is comprehensible because unlike atoms, molecules in general are not isotropic systems and its ionization dynamics can be strongly influenced by their alignment with respect to the laser field. For example, the ionization rate of nitrogen is 3~4 times greater when the molecular axis is aligned parallel with laser polarization rather than perpendicular [48,49].

Therefore, it is of great interest to investigate how THz radiation in two-color photoionization is affected by molecular alignment during tunneling ionization. This provides a better understanding of THz generation mechanism and in particular, the role of tunneling ionization in THz generation. To experimentally investigate this phenomenon, one can perform a double-pulse experiment. The first step is to prepare aligned molecules. Normally molecules are randomly oriented but can be aligned with moderately-intense laser excitation [50]. An ultrafast laser pulse provides an instantaneous torque to the molecules, making the molecular axes aligned along the laser polarization direction. After this initial kick, the molecules undergo periodical alignment and anti-alignment during the rotational period of the molecule. By ionizing the aligned molecules at the moment of alignment (anti-alignment) with intense two-color laser pulses, one can modulate the ionization rate, potentially enhancing THz emission.

In this chapter, we discuss the model of orientation-dependent ionization of molecules and molecular alignment induced by intense laser pulses. Later, we discuss our experiment work on studying THz radiation modulated by molecular alignment.

3.2 Photoionization of molecules

In the previous chapter, we discussed photoionization of atoms in strong laser fields. At the intensity of our interest, ~10^{14} W/cm^2, tunneling ionization is dominant and can be described by the ADK (Ammosov-Delone-Krainov) model. In principle, the ADK model is suitable for atomic gases such as Ar and Xe. Recently, Tong *et al*. extended the model to calculate the tunneling ionization rates of diatomic molecules [51], which is termed as a molecular (MO)-ADK model. Here, we provide a qualitative description of the model.

In the MO-ADK model, the ionization rate depends on the geometry of the charge distribution of valence electrons [52]. The right column in Figure 3.1 shows the molecular orbitals of several molecules (N_2, CO, CO_2, O_2, and C_2H_2). For N_2, the molecular orbital has σ symmetry, with its electron cloud preferentially distributed along the internuclear axis. Therefore, when the laser field is polarized along the internuclear axis, ionization enhances. However, when the laser field is applied perpendicular to the internuclear axis, ionization becomes strongly suppressed. The central column in Figure 3.1 shows calculated ionization rates for various molecules obtained by the MO-ADK model. In all cases, the angular distributions of ionization are strongly correlated with the molecular orbitals. This intuitive picture has been confirmed in experiments using COLTRIMS (Cold Target Recoil Ion Momentum Spectroscopy) [52]. As shown in Figure 3.1, the measured COLTRIMS results (left

column) agree well with the MO-ADK calculations (middle column) [52]. In short, the MO-ADK model provides a simple understanding of how the angular distribution of ionization can be affected by the molecular orbital structure.

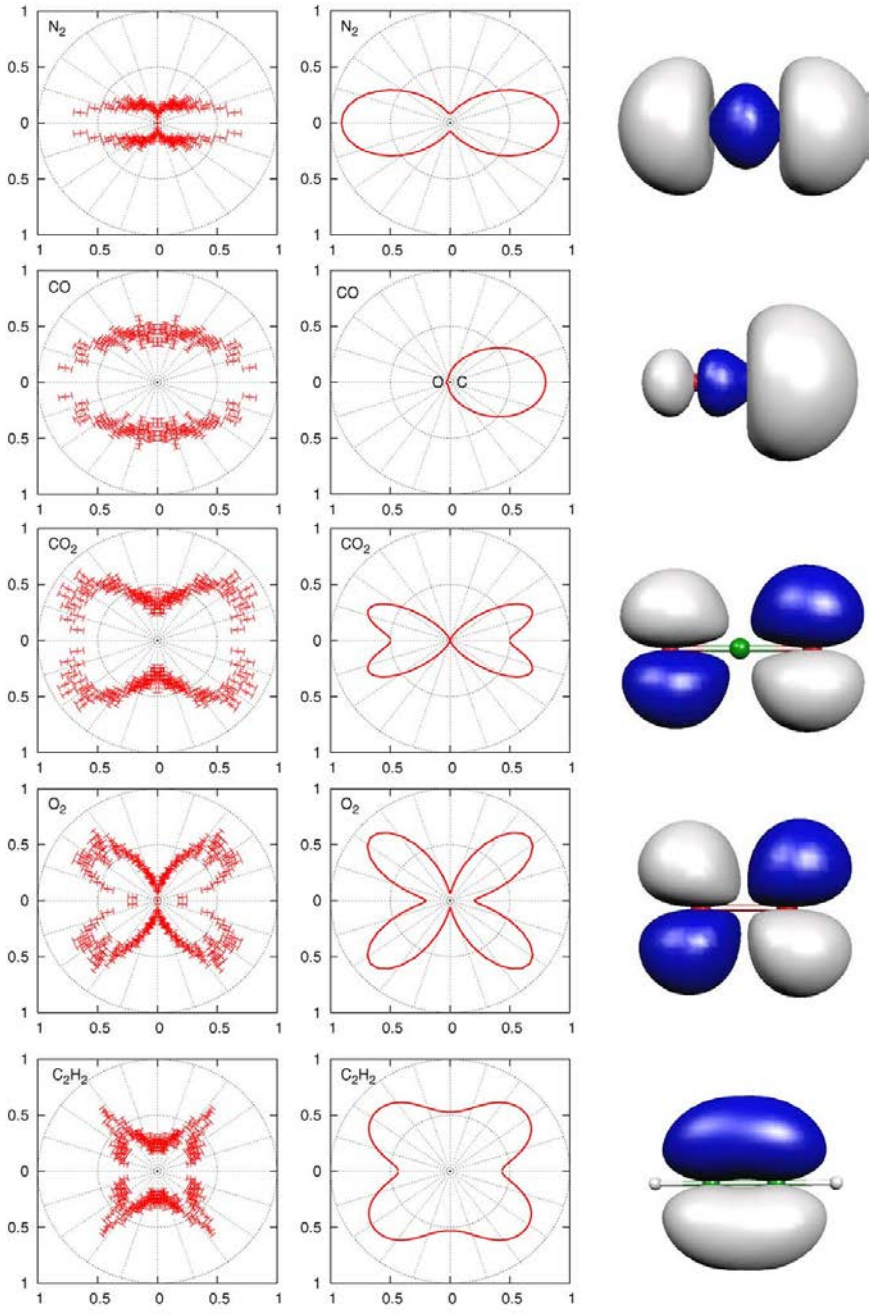

Figure 3.1 Comparison of measured angular distributions of ion fragmentation (left column) and alignment-dependent ionization rate (center column) calculated from the MO-ADK model for different gases. Right column shows the correspondent molecular orbitals (reprinted from [52]).

3.3 Molecular alignment by ultrafast laser pulses

When a molecule is placed in an electric field *E*, a small dipole moment $P = \boldsymbol{\alpha} \cdot \boldsymbol{E}$ is induced in the molecule, where α is the polarizability, which depends on the electron cloud distribution of the molecule. For a linear molecule such as N_2, O_2 or CO_2, the electron cloud distribution is not spherically symmetric. In this case, the polarizability can be described by a tensor $\boldsymbol{\alpha}$, which can be decomposed into two perpendicular components, with $\alpha_{\parallel}$ and $\alpha_{\perp}$ being the tensor along the major and minor axis of the molecule, respectively. In general, $\alpha_{\parallel}$ is larger than $\alpha_{\perp}$ because the electron cloud distributes more along the internuclear axis. When a linear molecule is placed in an electric field *E* with an angle, the induced dipole moment can be decomposed into the major ($\hat{e}_{\parallel}$) and minor ($\hat{e}_{\perp}$) axes,

$$\boldsymbol{p} = \boldsymbol{\alpha} \cdot \boldsymbol{E} = \alpha_{\perp} E_{\perp} \hat{e}_{\perp} + \alpha_{\parallel} E_{\parallel} \hat{e}_{\parallel} . \tag{3.1}$$

For a nonzero angle, the electric field exerts a torque $\boldsymbol{\tau} = \boldsymbol{p} \times \boldsymbol{E}$ on the molecule, rotating the molecule to be aligned with respect to the electric field.

For an ensemble of molecules, the degree of alignment is defined as $\left\langle \cos^2 \theta \right\rangle - 1/3$, where θ is the relative angle between the electric field and molecular major axis, and $\left\langle \cos^2 \theta \right\rangle$ is ensemble-averaged over the entire solid angles. For a random orientation, often observed in thermal equilibrium, $\left\langle \cos^2 \theta \right\rangle$ ~1/3 and the degree of alignment becomes zero. When the molecules are preferably aligned along the electric field direction, the degree of alignment becomes positive. When the molecules are preferentially aligned perpendicular to the electric field, which is called

"anti-aligned", then the degree of alignment becomes negative. The maximum degree of alignment is 2/3 whereas it is -1/3 for anti-alignment.

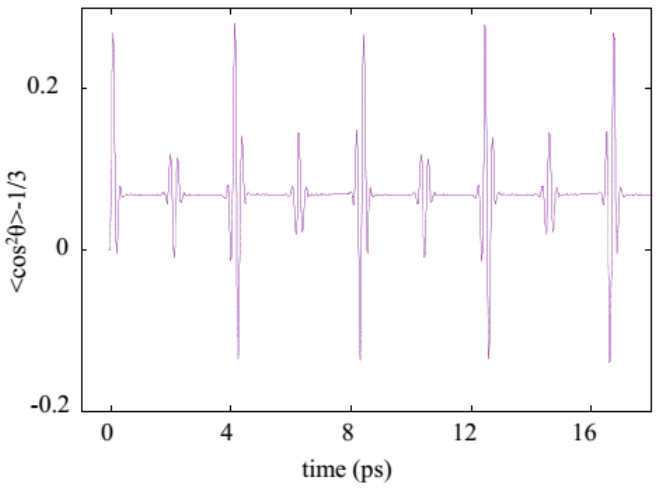

Figure 3.2 Calculated alignment degree of N_2 (room temperature) as a function of time, after excited by a laser pulse with peak laser intensity of 10^{14} W/cm^2.

When an ultrashort laser pulse interacts with an ensemble of molecules, the molecules exhibit initial alignment under the laser field and then undergo a series of alignment and anti-alignment even after the laser pulse disappears. This phenomenon is called "field-free alignment". Figure 3.2 shows a time evolution of the degree of alignment for an ensemble of N_2 molecules under excitation of a laser pulse with intensity of 10^{14} W/cm^2. As shown in the figure, the N_2 molecules undergo alignment and anti-alignment periodically, where the period is determined by the rotational constant of the molecule. In the case of N_2, the full revival period is 8.2 ps. During the rotational revivals, the alignment degree gradually decreases with time due to decoherence induced by collisions.

The understanding of field-free alignment requires a treatment of quantum mechanics [50]. An ultrashort laser pulse non-resonantly excites many rotational

modes of the molecule via Raman transitions, leaving the molecule in a coherent superposition of many rotational levels. Then the molecular wavepacket undergoes Rabi-type oscillations with periodic alignment and anti-alignment.

3.4 THz generation from aligned molecules

In the plasma current model [53], as discussed in Chapter 1, the far-field THz radiation arises from a time-varying electric current density $J(t)$ as

$$E_{THz} \propto \frac{dJ(t)}{dt} \approx ev_d(t)N_g w(t), \tag{3.2}$$

where e is the electron charge, $v_d(t)$ is the drift velocity of the electrons born at t, N_g is the gas density, and $w(t)$ is the ionization rate. For an ensemble of molecules, the ionization rate can be generally expressed as

$$w(t) = C\int w(\theta, E_L(t))A(\theta, t)d\theta, \tag{3.3}$$

where C is a constant, θ is the angle between the laser polarization and the molecular axis for linear molecules, $w(\theta, E_L)$ is the alignment-dependent ionization rate at the laser field E_L, and $A(\theta, t)$ is the alignment distribution at time t [49,54]. Using a MO-ADK model combined with molecular alignment, Zhao *et al*. showed that the ionization rate $w(t)$ for an ensemble of molecules nearly follows the degree of alignment, $\langle\cos^2\theta\rangle - 1/3$, for both N_2 and O_2 molecules at room temperature [54]. Based on this and Eq. (3.2), the far-field THz signal is expected to follow the ensemble average of molecular alignment.

3.5 Experiment

Our experimental set up is shown in Figure 3.3. An 800 nm, >5 mJ, 25 fs laser pulse is split into three beams—molecule alignment, THz generation, and THz detection (probe) beams. The energy of alignment and THz generation beams are 0.6 mJ and 2 mJ, respectively. Both of them are focused in air by a 15 cm lens, followed by a BBO crystal which generates second harmonic pulses. At the focal spot, air molecules undergo rotational revivals torqued by the alignment beam and then tunneling ionization by the THz generation beam. THz radiation is emitted in this ionization process. For optimal THz generation, the BBO position is optimized with respect to the focal spot, and the extraordinary axis of BBO is tuned at ~50° with respect to the incoming ω laser field (see Chapter 5). The emitted THz pulse is then transmitted through a high-density black polyethylene filter (1 mm) and focused by an off-axis parabolic mirror onto a 1-mm thick ZnTe crystal for electric-optical sampling (EOS) (see Appendix A) [8]. In general, the THz polarization is determined by 2-dimensional (2D) electron currents driven by two-color laser pulses having different polarization (see Chapter 5 for details) [56–58]. Here, we only detect THz radiation polarized along the optical probe polarization direction (linear).

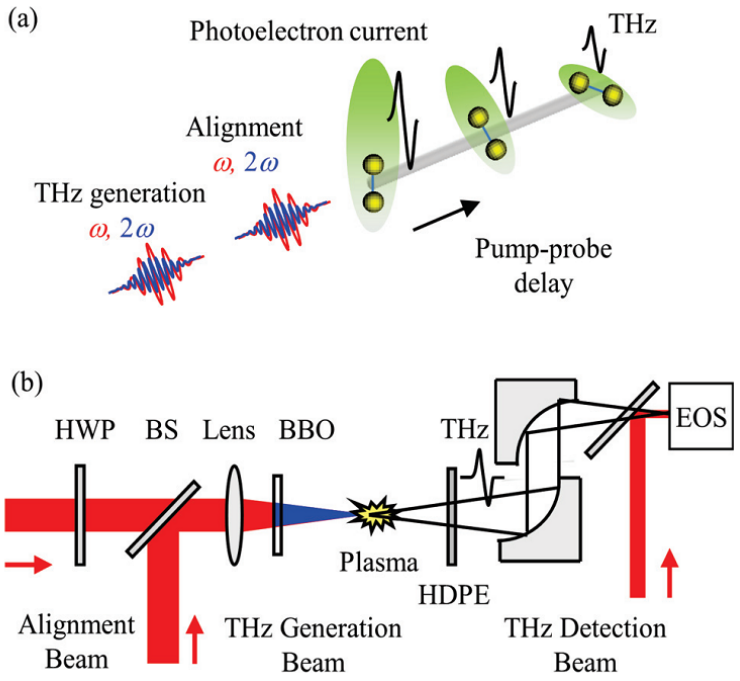

Figure 3.3. (a) Schematic of alignment-dependent photoionization of nitrogen molecules and resulting THz modulations in a pump-probe setup. (b) Experimental setup with three synchronous femtosecond laser beams for aligning molecules, generating and detecting THz radiation. HWP: half wave plate (optional), BS: beam splitter, BBO: β-barium borate crystal, HDPE: high-density polyethylene filter, EOS: electric-optical sampling for coherent THz detection.

3.6 Results

In the first experiment, we set the optical probe delay at the peak of THz pulse and vary the delay between the alignment and THz generation beams. By doing so, we can measure how the peak THz amplitude changes with molecular alignment. Figure 3.4(a) shows the measured THz amplitude modulation (line with crosses) and the simulated (solid line) alignment degree of O_2 and N_2. It is seen that the THz modulation strongly follows the combined molecular revival structure of O_2 and N_2. This shows that when the molecular axis is aligned parallel with the laser field, the ionization rate enhances, resulting in more THz radiation (vice versa for the perpendicular case). A noticeable discrepancy around $t = 0$ caused when the aligning

and THz generation beams superimpose in time and they both contribute to generate THz radiation. In fitting the experimental data in Figure 3.4(a), a ratio of 1:2 is used from the alignment degrees of O_2 and N_2. From the density ratio of O_2 and N_2 in ambient air (2:8), we get a ratio of 2:1 for the ensemble averaged ionization rate of O_2 and N_2, consistent with the simulated result in [54].

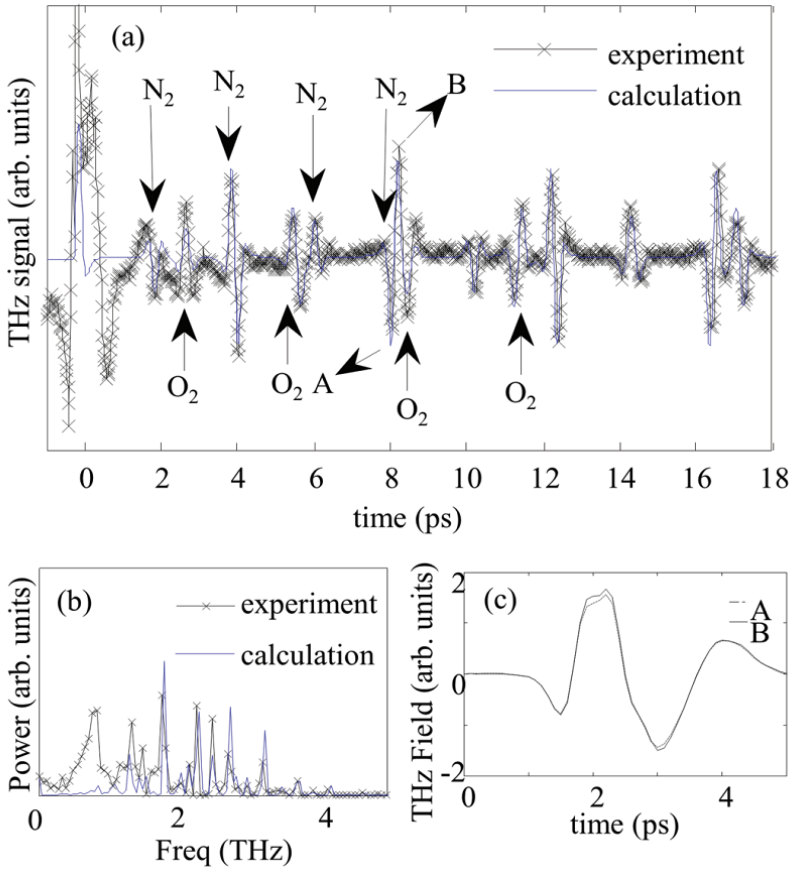

Figure 3.4 Measured (black line with crosses) and simulated (blue line) THz output modulations versus delays. (b) Fourier transforms of the experimental (black line with dots) and simulated (blue line) alignment parameters. (c) THz waveforms obtained at delays A (dashed line) and B (solid line) marked in Figure 3.4 (a).

We also obtained the Fourier transforms of the experimental data and calculation. The results are shown in Figure 3.4(b). The frequency at which the signal peaks is proportional to the energy difference between two adjacent Raman rotational levels, which is proportional to the rotational constant B (B_{N2} = 2.0 cm^{-1} and B_{O2} = 1.4

cm^{-1}) of the molecules. The magnitudes of the peaks are mainly corresponding to the population differences of the adjacent Raman rotational levels [59]. The Fourier transform of the alignment parameter tells us the population between two rotational level *j* and *j-2*, which provides a fingerprint of specified molecules.

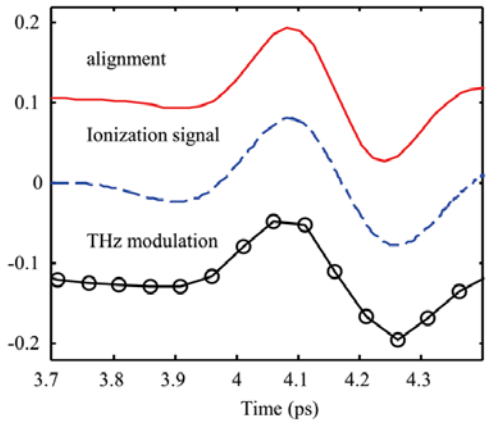

Figure 3.5 Simulated degree of alignment of N_2 at its half-revival period (red solid line), ionization signal retrieved from [54] (blue dashed line), and measured modulation of THz field (line with circles).

To understand how the THz waveform changes during molecular alignment, we obtain THz waveforms at two different alignment delays corresponding to the anti-aligned (A) and aligned (B) conditions of N_2 molecule around 8.2 ps, the full revival period of N_2. Figure 3.4(c) shows the measured THz waveforms. Although the amount of THz amplitude modulation is small (<10%), it clearly shows that the THz yield is enhanced when the molecular axis is parallel to the laser polarization rather than randomly oriented. In addition, the measured THz modulation around the half revival period of N_2 is co-plotted in Figure 3.5 with the simulated degree of alignment of N_2 (red solid line) and alignment-dependent N_2 ionization rate (blue dashed line) [54]. The good agreement between the ionization and THz curves supports the

molecular ionization model for THz generation. In particular, both show a slightly delayed negative peak at 4.25 ps compared to the alignment curve.

In another set of experiments, a half wave plate is inserted in the alignment beam path to rotate the polarization of the alignment beam from parallel to perpendicular. Figure 3.6 shows the experimental and simulated results for THz fields with two different polarization states. They are vertically offset for clarification. In both cases, the THz modulation signal follows the predicted ensemble averaged alignment except slow background signal drifts. It is seen that the THz modulation signal becomes reversed with orthogonal polarization. In particular, the signal at the full revival period of N_2 (8.2 ps at the dotted line) shows that the ensemble averaged ionization rate is 1.6 times higher with parallel alignment (θ = 0°) compared to perpendicular alignment (θ = 90°). This agrees well with the measurement in [49] under similar conditions. We note that the ionization rate ratio obtained here is for an ensemble of aligned molecules of $\langle\cos^2\theta\rangle \sim 0.6$. For the pure angle-dependent ionization rate, $w(\theta, E_L)$, the ratio becomes 3~4 after deconvolving Eq. (3.3) with a calculated or measured alignment distribution function $A(\theta)$ [48,49].

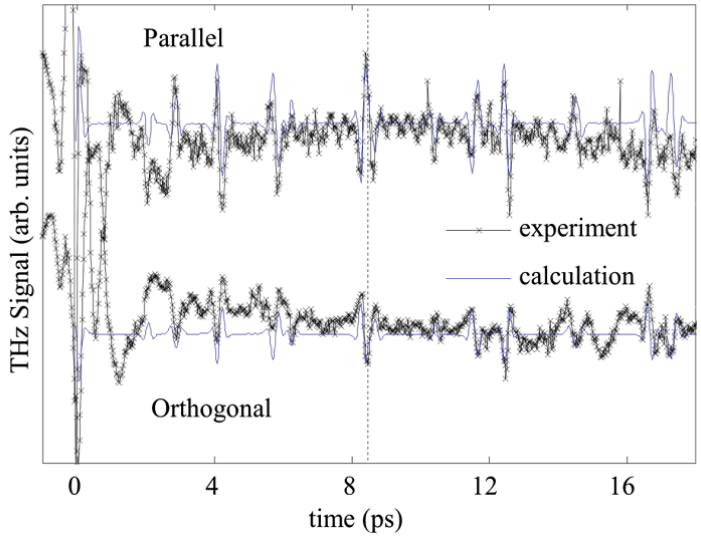

Figure 3.6 Measured (line with crosses) and simulated (blue line) THz field modulations with parallel (upper) and orthogonal (lower) polarization of the alignment beam with respect to the THz generation beam.

3.7 Conclusion

In conclusion, we have investigated how the molecular alignment of O_2 and N_2 can affect THz radiation in two-color photoionization. Our experimental results show THz radiation is extremely sensitive to the alignment of molecules during tunneling ionization. This can be explained by alignment-dependent ionization in the context of the plasma current model, in which molecules aligned along the laser field undergo more ionization, enhancing their near-field plasma currents and far-field THz radiation.

Chapter 4 : Off-Axis Phase-Matching of THz Generation from Two-Color Laser Produced Plasma

4.1 Introduction

Phase matching is crucial for efficient frequency conversion in many nonlinear processes. So far various phase-matching conditions have been studied at a broad range of electromagnetic (EM) frequencies, including infrared, optical [60], extreme ultraviolet light [61] and soft x-ray [62]. At terahertz (THz) frequencies, there have been several approaches to achieve phase- matching conditions [63–65]. Zinc telluride (ZnTe) crystals are commonly used to match the group velocity of Ti:sapphire lasers pulses with the phase velocity of THz waves in optical rectification processes [63]. Recently, quasi- and noncollinear phase-matching has been demonstrated in lithium niobate ($LiNbO_3$) crystals with periodical crystal poling [64] or tilted pulse front excitation [66] methods, respectively, where the conventional phase-matching scheme described above does not simply apply. In particular, the latter method can produce high energy (tens of microjoules) THz radiation, with optical to THz energy conversion efficiencies approaching nearly 1% [65]. These schemes, however, are vulnerable to material damage when excited by high-power lasers, which fundamentally limits THz energy scaling.

By contrast, material damage is almost absent in plasma-based THz sources. In particular, femtosecond laser-produced plasma is an ideal medium for scalable THz generation if phase matching can be achieved in plasmas. Previously, Cherenkov-type phase matching was reported in single-color, laser-produced plasmas [67], but the overall conversion efficiency is extremely low because of its relatively poor nonlinear effect in single-color photoionization.

As discussed in chapter 1, the efficiency can be greatly enhanced by creating plasmas with two-color laser focusing [19,21,57,68,69] . In this scheme, the resulting THz radiation amplitude is sensitive to the relative phase θ between the ω and 2ω pulses in the plasma. Many experiments have shown that the THz amplitude scales as $E_{\mathrm{THz}} \propto \sin\theta$ [17–19,69,70], assuming constant θ over the entire plasma length (typically <10 mm). However, long plasma filaments ranging from a few centimeters to tens of meters can be formed via femtosecond filamentation in air [71]. In this case, the relative phase θ varies along the filament direction, modulating the amplitude and polarity of local THz waves. Because of this, no THz enhancement was previously predicted in the forward direction [72].

In this Chapter, we report a new type of phase-matching condition for efficient THz generation in two-color filamentation. In this scheme, phase matching naturally occurs in the off-axis direction, resulting in a donut-shape profile in the far field. In addition, this type of phase-matching can lead to more THz output power with increasing plasma length.

4.2 Concept of off-axis phase matching in THz generation.

Figure 4.1 shows a schematic of THz generation along a long plasma filament. As two-color pulses (ω and 2ω) propagates along the filament, the relative phase changes as $\theta = 2\omega(n_\omega - n_{2\omega})l / c + \theta_0$, where $n_{\omega,2\omega}$ is the refractive index of plasma filament at ω and 2ω frequencies, contributed from both air and plasma dispersion ($n_{filament,\omega} = n_{air,\omega} + n_{plasma,\omega}$); l is the filament length; and θ_0 is the relative phase at the starting point of the filament, determined by the frequency doubling process and air

dispersion before the plasma filament. Here, $n_{plasma,\omega} \approx \sqrt{1-\omega_p^2/\omega^2}$, where ω_p is the plasma frequency (for $n_{air,\omega}$, see [38]). Because of the air-plasma dispersion, the relative phase θ varies over the filament length. Here, the dephasing length, over which the resulting THz polarity remains the same ($0 \le \theta \le \pi$), is given by $l_d = (\lambda/2)(n_\omega - n_{2\omega})^{-1}$, where λ is the wavelength at ω. For example, for pure (no plasma) atmospheric air, the dephasing length is $l_d \approx 25$ mm at $\lambda = 800$ nm. For a filament with electron density of $N_e \sim 10^{16}$ cm^{-3} [73] in atmospheric air (~10^{19} cm^{-3}), $l_d \approx 22$ mm. Because of this dephasing effect, an oscillatory THz output is expected in the forward direction as the relative phase continuously varies along the filament [72]. This leads to maximal THz generation with filament length $l \approx l_d$.

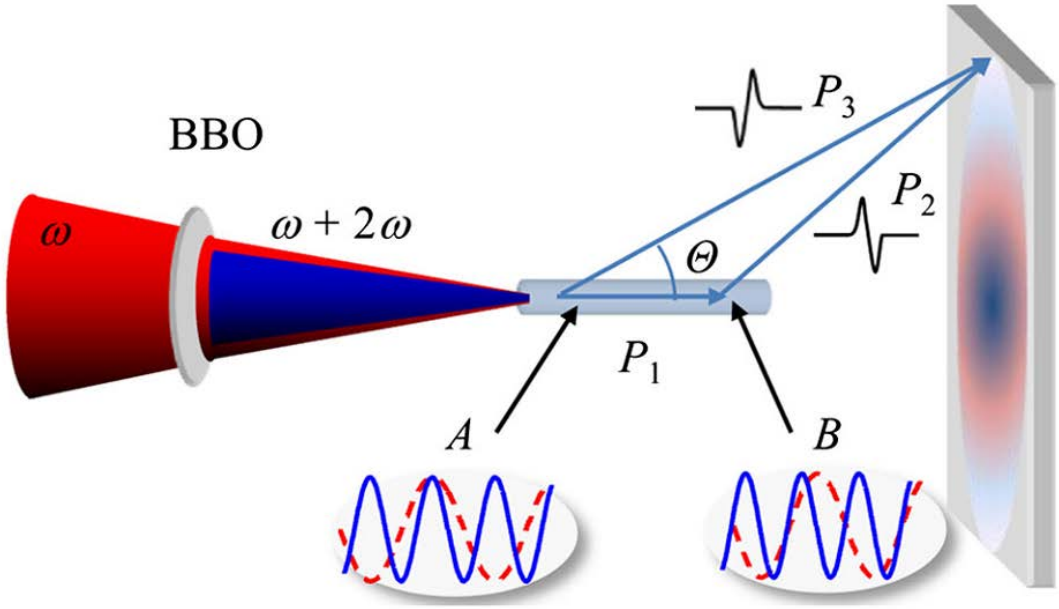

Figure 4.1 Schematic of THz emission from a long, two-color laser-produced filament. The phase slippage between 800 nm (red curves) and 400 nm (blue curves) pulses along the filament results in a periodic oscillation of microscopic current amplitude and polarity. The resulting far-field THz radiation is determined by interference between the waves emitted from the local sources along the filament.

However, natural phase matching can occur in the off-axis direction. This can be explained by a simple interference effect. For a plasma filament comparable to or longer than the dephasing length, l_d, the THz waves produced along the filament have both positive and negative polarities as shown in Figure 4.1. For example, consider the polarity is positive at point *A* and negative at point *B* (l_d distance away from *A*). The waves produced at points *A* and *B* interfere constructively if the path difference is $\Delta l = P_3 - (P_1 + P_2) = (m + 1/2)\Gamma$, where $m = 0, 1, 2, ...$ and Γ is the THz wavelength. With $m = 0$, the angle for constructive interference is given by $\cos\Theta \approx 1 - \Gamma/(2l_d)$. For $l_d = 20$ mm and $\Gamma = 200$ μm, the emission peaks at $\Theta \sim 6°$. Note that this type of off-axis phase matching is only achieved when the radiation wavelength, Γ, is longer than the source transverse size, *D*, but shorter than the dephasing length ($D < \Gamma < l_d$). For typical air filamentation, $D < 100$ μm and $l_d \approx 22$ mm, which naturally fulfills the phase-matching condition. However, the constraint is not satisfied for conventional optical second harmonic or high harmonic generation (because $\Gamma/D < 0.1$) or THz generation in nonlinear crystals (because $D > \Gamma$ or $\Gamma > l_d$).

4.3 Simulation model

For a better understanding of THz emission from long plasma filaments, we develop a 2D THz generation and propagation model. In this model, the local THz source at position r' can be represented by the nonlinear polarization $\tilde{P}$ as

$$\tilde{P}\left(r^{'},\Omega\right) \propto \tilde{A}\left(r^{'},\Omega\right)\sin\left(\theta(z')\right)\exp\left(in_g k_\omega z^{'} - i\Omega t\right), \tag{4.1}$$

where $\tilde{A}$ is the local THz amplitude at frequency Ω, given by the microscopic plasma current model [53]. The second term provides a phase-dependent THz amplitude

modulation along the filament direction z' owing to the phase mismatch between ω and 2ω pulses. The last term represents the velocity walk-off between the optical and THz pulse, where n_g is the optical group velocity index of refraction in the filament. The THz far-field is then expressed by integrating the contributions from all local sources over the entire filament plasma volume as

$$E(r,\Omega) \propto \int_V d^3r' \frac{\tilde{P}\left(r',\Omega\right)e^{i\,k_{THz}|r-r'|}}{|r-r'|}. \tag{4.2}$$

For simplicity, the filament is approximated as uniform cylindrical plasma with a cross section of πa^2 and length l. At a distance far longer than the filament length ($|\boldsymbol{r} - \boldsymbol{r}'| >> |\boldsymbol{r}'|$), $\exp(ik_{THz}|\boldsymbol{r} - \boldsymbol{r}'|)/|\boldsymbol{r} - \boldsymbol{r}'| \approx \exp[ik_{THz}(r - \boldsymbol{r}\cdot\boldsymbol{r}'/r)]/r$. The integral in the cylindrical coordinate is [74]

$$\begin{aligned} E(r,\Omega) \propto \tilde{A}\left(\boldsymbol{r}',\Omega\right)\frac{\exp\left(ik_{THz}r - i\Omega t\right)}{r}\int_0^a d\rho' \int_0^{2\pi} \rho' d\varphi' e^{-ik_{THz}\rho'\cos\varphi\sin\Theta} \\ \times\left\{\left[\int_{-l/2}^{l/2} dz' e^{-ik_{THz}z'\left(n_g+\frac{\Gamma}{2l_d}-\cos(\Theta)\right)} e^{i\theta_0}\right] - \left[\int_{-l/2}^{l/2} dz' e^{-ik_{THz}z'\left(n_g-\frac{\Gamma}{2l_d}-\cos(\Theta)\right)} e^{-i\theta_0}\right]\right\}. \end{aligned} \tag{4.3}$$

The far-field THz intensity profile can be approximated as [74]

$$\left|E\left(r,\Theta,\Omega\right)\right|^2 \propto \left|\tilde{A}\left(r',\Omega\right)\right|^2 \frac{(\pi a^2)^2 l^2}{r^2}\left(\kappa_1^2 + \kappa_2^2 + 2\kappa_1\kappa_2\cos\left(2\theta_0 + \pi\right)\right)\left(\frac{2J_1\left(\beta\right)}{\beta}\right)^2, \tag{4.4}$$

where $\kappa_{1,2} = \dfrac{\sin(\alpha_{1,2})}{\alpha_{1,2}}$, $\alpha_{1,2} = \dfrac{k_{THz}l}{2}[n_g \pm \dfrac{\Gamma}{2l_d} - \cos\left(\Theta\right)]$, $\beta = \dfrac{2\pi a}{\lambda}\sin\left(\Theta\right)$, and the last term is the circular diffraction term. The third term provides a phase-matching condition for efficient THz generation. It depends on two terms α_1 and α_2, instead of one term in most cases, due to the sinusoidal dependence of the local emitters on the phase between the two optical pulses. The condition provides the phase-matching

angle, Θ_p, for maximal THz generation, given by $\cos\left(\Theta_p\right)=1-\frac{\lambda}{2l_d}$ for weakly ionized plasma filaments ($n_g \approx 1$). This is the same condition obtained with the simple interference picture described before. Here, Θ_p is sensitive to the dephasing length and varies with the THz frequency. We note that the THz yield at $\Theta = \Theta_p$ increases with l^2, but total THz yield $\int \left|E\left(r,\Theta,\Omega\right)\right|^2 \sin\Theta d\Theta$ does not simply increase with l^2 because the angle-dependent phase-matching term.

Figure 4.2(a) shows the angular distributions at 1 THz for $l = l_d$, $2l_d$, and $3l_d$. The THz profile transforms from on axis to off-axis when the plasma length is longer than the dephasing length. Figure 4.2(b) shows that for $l > l_d$, Θ_p tends to decrease with increasing THz frequency. Figure 4.2(c) shows the angle-dependent yield $\left|E\left(r,\Theta,\Omega\right)\right|^2$ at 1 THz as a function of increasing filament length for various angles. At $\Theta \sim 7°$, the yield increases almost with l^2 as predicted in Eq. (4.4), but it drops after passing the phase-matching angle (see $\Theta = 8°$). We also calculate how the total yield at 1 THz depends on the length of the plasma. As shown in Figure 4.2(d), when the plasma is shorter than the dephasing length ($l << l_d$), the yield is greatly sensitive to the initial phase, consistent with the microscopic behavior [17–19,69]. However, when the plasma length becomes longer ($l \geq l_d$), the yield increases almost linearly regardless of the initial phase. Here, the constraint $D < \Gamma < l_d$ needs to be satisfied. For example, the total yield at 1 THz with a large source diameter D = 2 mm ($\Gamma/D \sim 0.15$) shows only an oscillatory behavior (no overall enhancement) with increasing filament length [see Figure 4.2(e)]. With a typical filament diameter ($D \sim 0.1$ mm),

the phase-matching condition is well satisfied at low THz frequencies [see Figure 4.2(f)].

The model, however, has several limits. It assumes cylindrical, uniform plasma-density filaments and excludes THz absorption and refraction inside the filaments. It also assumes luminal THz phase velocities and optical group velocities in free space. A recent simulation shows that when optical group velocities are faster than THz phase velocities, an optical Cherenkov radiation can happened in the case and resulted in off-axis phase-matching [75]. We note that our non-collinear and ω and 2ω polarization scheme can produce, in general, elliptically polarized THz polarization [56,57]. It also ignores self-phase modulation in air and spectral blue shifts via tunneling ionization occurring over the entire plasma filament. Nonetheless, as our experimental results indicated, our simple model well describes the measured THz emission yields and angular profiles, providing a physical insight into macroscopic THz propagation and enhancement processes in plasmas.

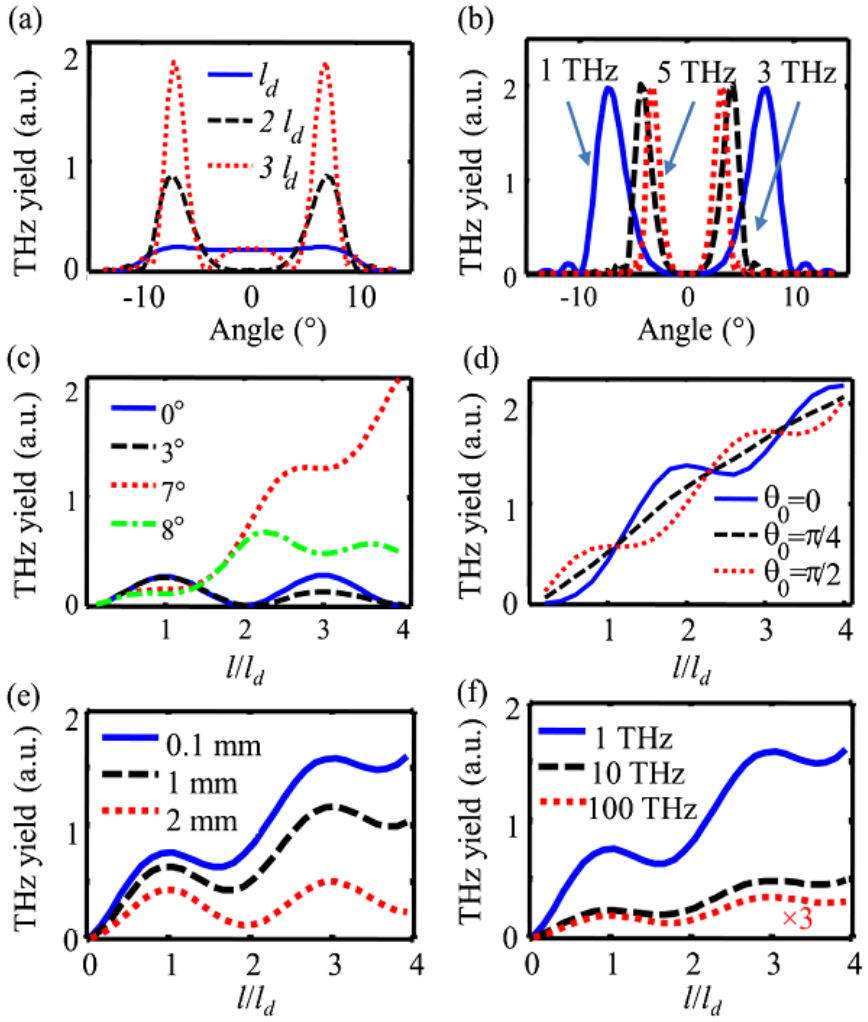

Figure 4.2 Simulation results for (a) THz profiles with different plasma length: $l = l_d$, $2\ l_d$, and $3\ l_d$ at 1 THz, (b) far-field THz profiles at three different frequencies: 1, 3, and 5 THz; (c) THz yield versus plasma length at various emission angles: Θ = 0°, 3°, 7°, and 8° at 1 THz; (d) total THz yield versus plasma length with different initial phases θ_0 = 0, π/4, and π/2 at 1 THz. Simulated THz yields with increasing plasma length normalized by the dephasing length for (e) three different filament diameters (0.1, 1, 2 mm) at 1 THz emission and (f) 0.1 mm filament diameter at 1, 10, and 100 THz radiation emission.

4.4. Experiments and results

To confirm phase-matched THz generation experimentally, a femtosecond laser system capable of delivering 25 *fs*, 6 mJ pulses at a repetition rate of 1 kHz is used. The laser pulses are focused by a lens, followed by, a 100 μm thick BBO (type-I) crystal which generates second harmonics (see Figure 4.1). Both fundamental and

second harmonic are focused in ambient air, creating a plasma filament. THz radiation emitted from the filament is detected by a pyroelectric detector. A silicon filter is used to block unwanted optical and infrared light. Additional filters are used to characterize THz profiles at different frequency bands: a germanium wafer is used to detect THz frequencies mostly at <10 THz, whereas a 3-mm thick Teflon window is used as a low pass filter to detect <3 THz. For THz imaging, the pyroelectric detector is raster scanned over 5 cm × 3.5 cm, which provides a detection angle of ~10°.

THz profiles are measured with two different plasma lengths. In the first set of experiments, the laser energy is limited to ~1.3 mJ with a beam size of 5 mm, and a lens of f = 15 cm is used to create relatively short plasma (~10 mm). The measured far-field THz profiles are shown in Figure 4.3(a) and 4.3(b) at high (germanium filter) and low (Teflon filter) THz frequencies, respectively. With laser energy of 5 mJ, beam diameter of 10 mm, and lens with f = 300 mm, a plasma filament longer than ~40 mm is created. The corresponding THz profiles are shown in Figure 4.3(c) and 4.3(d), at low and high THz frequencies, respectively. Here, the emission angle is ~5° in Figure 4.3(c). In the limit where the plasma filament length is much shorter than the dephasing length l_d, all THz waves have the same polarity and constructive interference in the forward direction, producing THz radiation peaked on axis. Such trend is somewhat shown in Figure 4.3(a), obtained with $l \leq l_d$. In this case, the yield, however, is much lower compared to the long filament case in Figure 4.3(c)-(d). We performed simulation based on Eq. (4.4) to examine our experimental results. Figure 4.3(e)-(f) show the simulated THz radiation profiles obtained from Eq. (4.4) under the

experimental conditions of Figure 4.3(c)-(d). The conical emission for $l \geq l_d$ is well reproduced in Figure 4.3(e)-(f) with $\Theta_p \sim 6°$, consistent with the measured peak radiation angle.

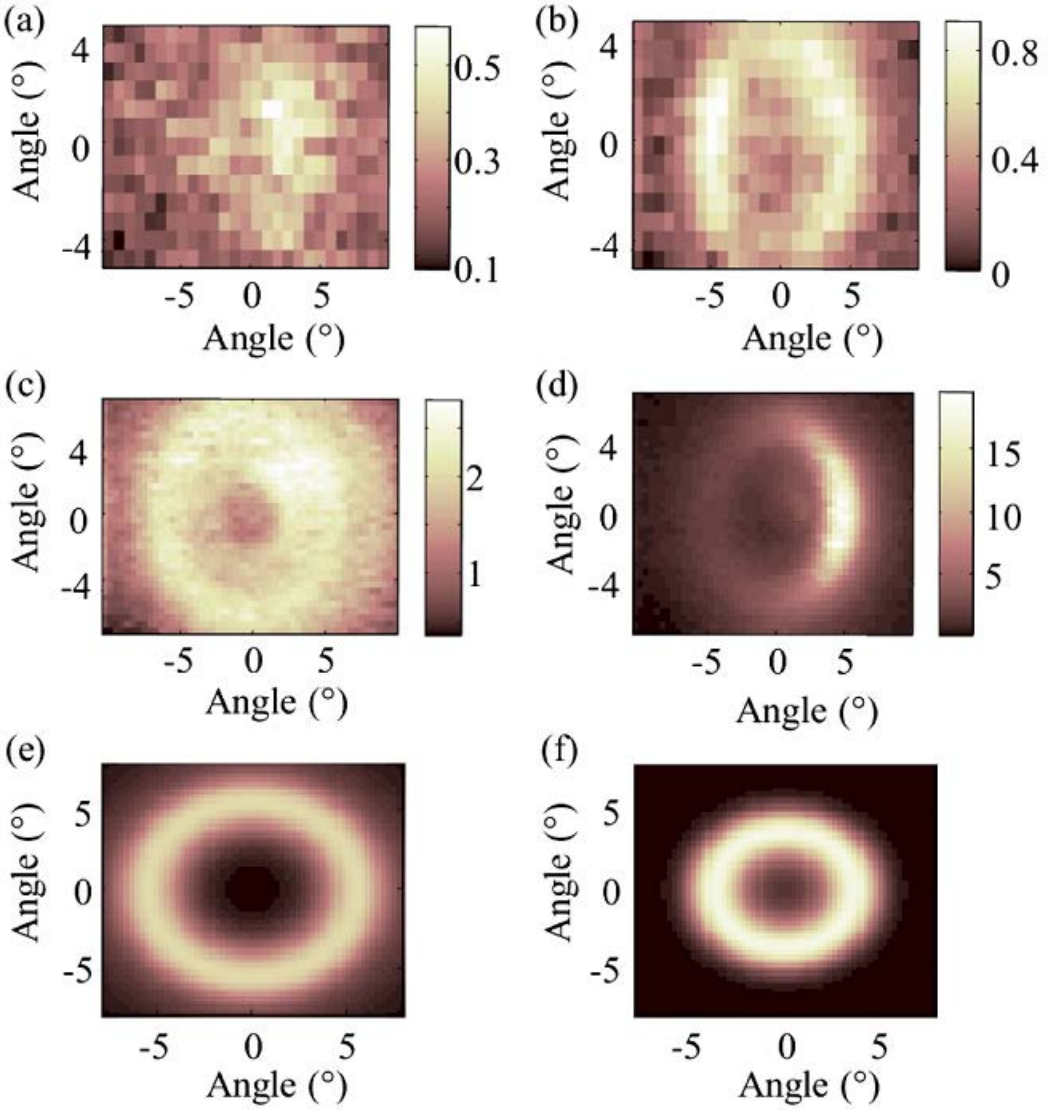

Figure 4.3 Measured far-field THz radiation profiles obtained with (a), (b) 10 mm long and (c), (d) 40 mm long filaments, all obtained by raster scanning of a pyroelectric detector with a silicon filter. Additional Teflon (a), (c) and germanium (b), (d) filters are used for low (<3 THz) and high (<10 THz) frequency band transmission. (e)-(f) are simulated THz profiles for the long filament case.

We also examine the radiation profiles of THz waves after being focused by a pair of parabolic mirrors. Figure 4.4 shows the measured profiles at three different axial positions, (a) -8 mm before, (b) at, and (c) 8 mm after the focal plane, all obtained with the 3-mm thick Teflon filter. Unlike the conical radiation profiles shown in Figure 4.3, the focused THz intensity is peaked on axis, confirming previous observations [76,77]. In Figure 4.4(b), the spot diameter is ~2 mm with an estimated peak field of ~50 kV/cm at <3 THz. This transition can be explained by propagation of Bessel–Gauss beam [78,79].

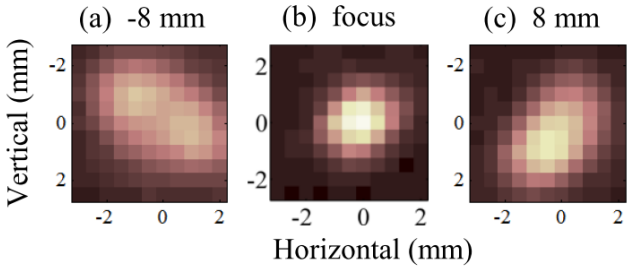

Figure 4.4 Focused THz radiation profiles obtained at (a) 8 mm before, (b) near, and (c) 8mm after the focal plane, all obtained with a 3-mm Teflon filter before the detector. Unlike the far-field profiles shown in Figure 4.3, the focused radiation peaks on axis.

We also measure how the total THz yield scales with the plasma length. A lens with f = 1.5 m is used to produce ~100 mm long plasma filaments. The resulting THz radiation is collected by a pair of parabolic mirrors and focused into the pyroelectric detector. An iris with an aperture diameter of ~2 mm is used to block the THz waves emitted in front of the iris, while the THz waves generated behind the iris are being unblocked and detected (see the inset in Figure 4.5) [68,72]. Here, THz transmission through the aperture is relatively small and thus ignored. By moving the iris along the filament, we can measure the effective plasma length responsible for the detected THz radiation. The result is shown in Figure 4.5. It shows that the THz yield

increases with the effective plasma length, regardless of the initial relative phase. Here, we tried three different BBO positions to provide $\theta_0 \approx 0$, $\pi/4$ or $\pi/2$ [69]. Figure 4.5 shows that the yield continuously increases over the entire scanned length ($l \approx 700$ mm), longer than 3 times the estimated dephasing length. This suggests we can continuously enhance the THz output by simply increasing the filament length, until the ω and 2ω pulses do not temporally overlap due to plasma dispersion. This gives a theoretical limit of ~4 m. We note that the saturation that appeared at ~70 mm is attributed to noncollected THz radiation emitted at the front part of the filament due to our limited collection angle.

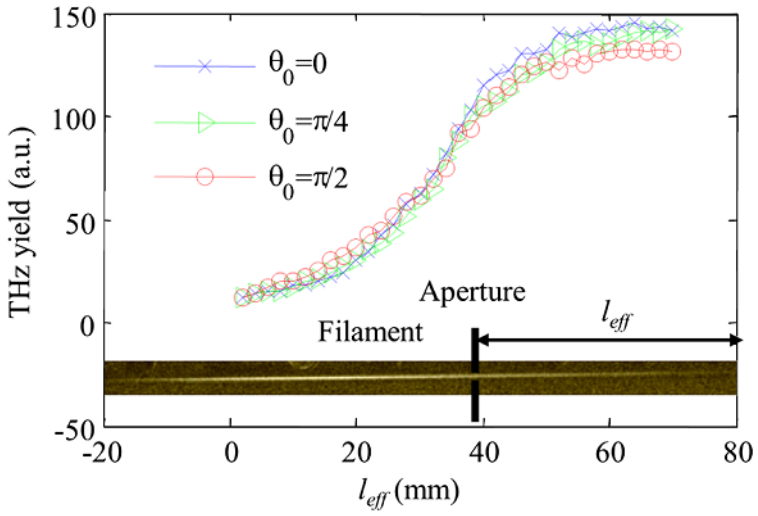

Figure 4.5 Far-field THz yield as a function of plasma filament length. The inset shows a luminescent image of a filament created by two-color laser pulses propagating from left to right. The measurements were done at three different BBO positions, representing three different initial phase differences: 0, π/4, and π/2.

4.5 Conclusion

In conclusion, we discover phase-matched THz generation in elongated two-color filamentation. In particular, we find the THz yields and angular distributions are greatly sensitive to the filament and dephasing length. Simultaneously, the yield

increases almost linearly with the plasma filament length as a result of quasi-phase matching. Because of this, one can effectively increase THz output by simply extending the plasma filament length. This method can overcome the saturation effect previously reported [21,69], mainly caused by overdense plasma creation and laser intensity clamping in filamentation.

Chapter 5 : Elliptically-Polarized THz Generation from Two-Color Laser Produced Plasma

5.1 Introduction

In the previous chapters, we have discussed THz emission from two-color laser pulses polarized in the same direction. In this case, the resulting THz radiation follows the same polarization direction. For simplicity, most two-color schemes adopt an in-line second harmonic generation arrangement where the frequency doubling crystal (type-I BBO crystal in our experiments) is azimuthally oriented such that the fundamental (ω) field has a component parallel to the second harmonic (2ω) field. In this setting, the polarization of ω and 2ω is not parallel to each other and the resulting THz pulse does not necessarily follow the polarization of ω or 2ω [56–58,80–82]. Further experiments show that THz polarization is often elliptical [80–82]. This ellipticity is either attributed to the finite length [80] or birefringence [81] of plasma. However, there is a lack of experimental proof and theoretical model to fully explain the emergence of THz ellipticity.

In our previous work, THz polarization is understood in the context of 2-dimensional (2D) plasma current model, in which two orthogonal plasma currents driven by the laser fields determine the far-field THz amplitude and polarization [58]. This microscopic (single-atom) model, however, predicts THz radiation solely polarized along the direction of the current vector sum. In this chapter, we extend the 2D plasma current model by including a macroscopic laser-THz propagation effect, which provides a basis for elliptically polarized THz pulse generation.

In general, the single-atom picture discussed in Chapter 1 can be applied to short (~millimeters) plasma lengths. However, when the plasma extends over

centimeters [71,73,83], the single-atom picture loses its validity. First, due to air-plasma dispersion, the relative phase, θ, between the ω and 2ω pulses changes along the plasma. Furthermore, the 2ω pulse experiences a cross-phase modulation (XPM) induced by the stronger ω pulse and changes its polarization during propagation [84,85]. These two parameters, θ and the polarization states of the optical pulses, have shown to affect the resultant THz polarization [58]. The modulations of these two parameters in turn change the direction of the local plasma current (thus THz polarization). Simultaneously, the optical and THz pulses propagate with different velocities in plasma [86], causing the local THz waves emitted from different parts of the plasma to arrive at different times in the far field. This effect is not considered in the previous models [80,81]. These two combined effects construct a THz pulse in the far field whose polarization direction rotates with time (see Figure 5.1).

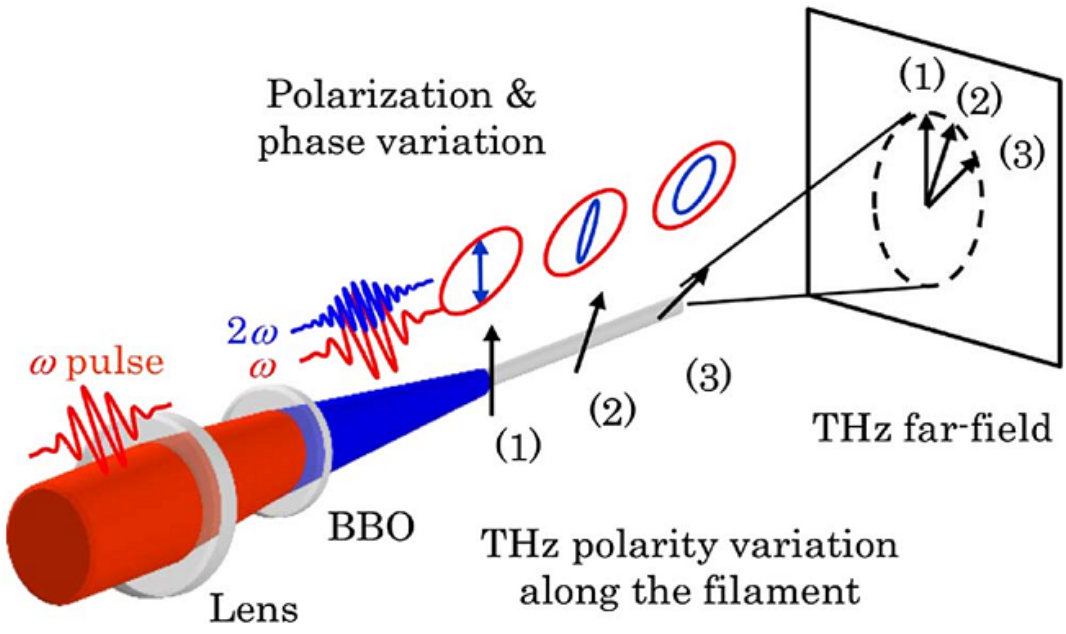

Figure 5.1 Schematic of two-color (ω and 2ω) laser pulse propagation and THz polarization rotation. The THz far-field is constructed from successive time-delayed THz waves emitted with varying polarization.

We first describe our 2-D plasma current model developed in [58] . Then, we discuss the propagation effects of two-color laser and THz pulses during THz generation process and how elliptical THz polarization can arise from those effects. Finally, we will describe our experimental settings and results which support our simple model in explaining elliptical THz polarization.

5.2 Two-dimensional plasma current model

In Section 1.3, we described the plasma current model to explain THz generation by two-color laser pulses with co-linear polarization. In this section, we extend the plasma current model [58] to consider two-color laser pulses with non-collinear polarization.

First, we discuss second harmonic generation in a BBO (Beta-Barium borate) crystal, one of nonlinear crystals widely used for efficient second harmonic

generation, to understand the properties of both fundamental and second harmonic laser pulses as they propagate in BBO.

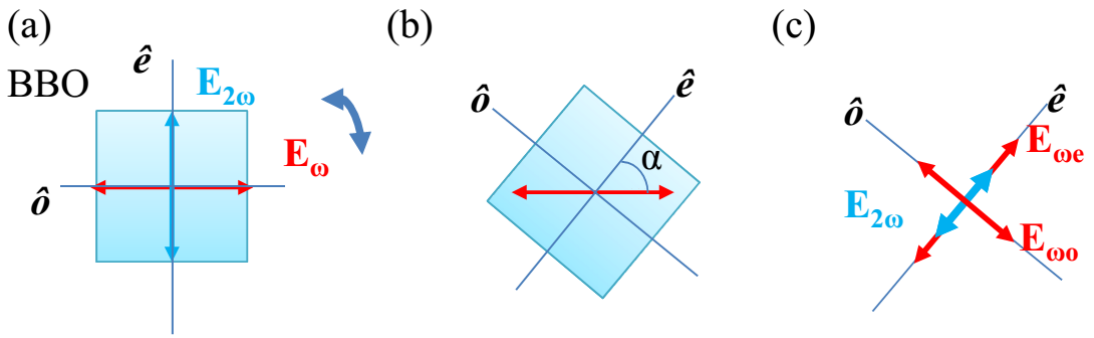

Figure 5.2 (a) Optimal second harmonic generation (SHG) occurs when E_ω is parallel to the o-axis of BBO, and generated $E_{2\omega}$ is polarized along the e-axis of BBO. (b) BBO is azimuthally rotated by an angle α such that E_ω has a component parallel to $E_{2\omega}$ (see (c)).

BBO has negative uniaxial birefringence with a crystal cut around 29 degrees for type-I phase-matching at a fundamental (ω) wavelength of 800 nm. A phase-matched second harmonic can be generated when the incoming ω pulse is polarized along the ordinary axis (*o*-axis) of the BBO crystal (see Figure 5.2). The produced $E_{2\omega}$ is polarized along the extraordinary axis (*e*-axis) of BBO. Under this perfect phase-matching condition, E_ω and $E_{2\omega}$ are polarized perpendicular to each other.

When the BBO crystal is azimuthally rotated to a nonzero angle (see Figure 5.2(b)), the incoming ω pulse can be decomposed into two components, $E_{\omega e}$ and $E_{\omega o}$, polarized along the *e*- and *o*-axis, respectively. Due to the birefringence of BBO, these two components acquire a phase difference $\varphi = \omega(n_{\omega e} - n_{\omega o})l / c$ after propagating through the BBO with thickness *l*, where $n_{\omega e}$ and $n_{\omega o}$ is the refractive index of BBO for ω pulses polarized along the *e*- and *o*-axis, respectively. After passing through the BBO crystal, the ω pulse becomes elliptically polarized whereas the produced $E_{2\omega}$ pulse is polarized along the *e*-axis. Here, the conversion efficiency is proportional to

the intensity of $E_{\omega o}$. The relative phase difference θ_0 between $E_{\omega e}(t)$ and $E_{2\omega}(t)$ can be controlled by the distance between the focal point and the crystal. In general, the two-color laser field $\vec{E}_L(t)$ after propagating through the BBO crystal can be presented as:

$$\vec{E}_L(t) = \begin{pmatrix} E_e(t) \\ E_o(t) \end{pmatrix} = \begin{pmatrix} E_{\omega e}\cos(\omega t) \\ E_{\omega o}\cos(\omega t + \varphi) \end{pmatrix} + \begin{pmatrix} E_{2\omega}\cos(2\omega t + \theta_0) \\ 0 \end{pmatrix}. \tag{5.1}$$

When the laser pulses are focused into air, the intense field ionizes air molecules, with ionization rates given by the Ammosov-Delone-Krainov (ADK) tunneling model introduced in Chapter 1,

$$w(t) = 4\omega_a \left(\frac{E_a}{|E_L(t)|} \right) \exp\left(-\frac{2}{3} \frac{E_a}{|E_L(t)|} \right). \tag{5.2}$$

where $|E_L(t)| = \sqrt{E_e(t)^2 + E_o(t)^2}$. The electrons freed at $t = t'$ are subject to the 2-D electric field $\vec{E}_L(t)$, acquiring a drift velocity given by

$$\vec{v}(t) = -(e/m_e)\int_{t'}^{t} \vec{E}_L(t)dt. \tag{5.3}$$

Then the 2-D plasma current density can be calculated as

$$\vec{J}(t) = -\int e\vec{v}(t,t')dN_e(t'), \tag{5.4}$$

where $dN_e(t')$ is the electron density produced by ionization in the interval between t' and $t' + dt'$. This plasma current surge emits THz radiation, $\vec{E}_{THz} \propto d\vec{J}(t)/dt$ as discussed in Chapter 1. In the case of non-varying θ and φ over the entire pulse duration, the relative current densities along two axes always remain constant. This results in linear THz polarization whose angle is determined by the relative strengths between the plasma currents along the *e*- and *o*-axes.

5.3 Propagation of laser and THz pulses

The refractive index of a gas medium is usually isotropic due to the random orientation of molecules and atoms. However, when an intense laser beam propagates through a gas, it can induce birefringence by a strong optical-Kerr effect. This "wave-plate" effect was first discovered by Bejot *et al*. [84] and demonstrated by several other groups [87]. Physically, an intense laser pulse distorts the electronic distribution of atom or molecules, resulting in anisotropy in the refractive index, $\Delta n = (4n_2 / 3)I_\omega$, where n_2 is the nonlinear refractive index of the gas medium and I_ω is the intensity of the pump beam. A probe beam with wavelength of λ propagating through the medium experiences a phase shift of $\Delta\phi = \frac{2\pi}{\lambda}\frac{4n_2}{3}I_\omega l$, where l is the interaction length.

As shown in the previous section, the polarization of ω and 2ω after a BBO crystal is not parallel to each other. To simplify the picture, the coordinates is transformed to the major axis (x) of the incoming ω polarization as

$$\begin{pmatrix} E_x \\ E_y \end{pmatrix} = \begin{pmatrix} \cos\alpha & \sin\alpha \\ -\sin\alpha & \cos\alpha \end{pmatrix} \begin{pmatrix} E_e \\ E_o \end{pmatrix}, \tag{5.5}$$

where α is given by $\tan 2\alpha = 2E_{\omega e}E_{\omega o}\cos\varphi / (E^2_{\omega e} - E^2_{\omega o})$. As discussed above, the intense ω field induce a strong change in the refractive index along the x and y axes. This wave-plate effect modulates the phase of the weaker 2ω pulse, resulting in a phase difference of $\Delta\phi_{2\omega} = (2\pi/\lambda_{2\omega})n_2\Delta I_\omega z'$, after a propagation distance of z'. Here n_2 is the nonlinear refractive index of air and ΔI_ω is the intensity difference of ω components projected onto the x and y axes.

In parallel, the relative phase difference θ changes along the plasma due to dispersion as $\theta(z') = \omega(n_\omega - n_{2\omega})z'/c + \theta_0$, where $n_{\omega,2\omega}$ is the refractive index of plasma filament at ω and 2ω frequency, contributed from both air and plasma dispersion ($n_{filament,\omega} = n_{air,\omega} + n_{plasma,\omega}$). The laser pulse along the plasma can then be characterized as

$$\begin{pmatrix} E_x(z') \\ E_y(z') \end{pmatrix} = \begin{pmatrix} \cos\alpha & \sin\alpha \\ -\sin\alpha & \cos\alpha \end{pmatrix} \begin{pmatrix} E_{\omega e}\cos(\omega t) \\ E_{\omega o}\cos(\omega t + \varphi) \end{pmatrix} + \begin{pmatrix} \cos\alpha E_{2\omega}\cos(2\omega t + \theta(z')) \\ -\sin\alpha E_{2\omega}\cos(2\omega t + \theta(z') + \Delta\phi_{2\omega}(z')) \end{pmatrix} . \quad (5.6)$$

Once the laser fields are completely characterized along the plasma, the corresponding local THz fields can be computed in the 2-D plasma current model [58]. These local THz waves $\boldsymbol{e}_{\mathrm{THz}}(z', t)$ sum up in the far field and constitute an elliptical THz pulse as

$$\boldsymbol{E}_{THz}(t) \propto \int_0^l \boldsymbol{e}_{THz}(z', t)\exp(-ik_{THz}\Delta n z')dz' , \quad (5.7)$$

where l is the plasma length and Δn is the refractive index mismatch between the optical and THz pulses in air-plasma [86].

5.4 Experiment

To demonstrate elliptically polarized THz generation and detection, an amplified Ti: sapphire laser system capable of producing 800 nm, <30 fs pulses at 1 kHz were used for our experiment. The energy of THz generation beam is ~3 mJ. The beam is focused in air by a 25-cm focal length lens, followed by a 0.1 mm thick beta-barium oxide (BBO) crystal which generates second harmonic pulses. The BBO crystal is adjusted to orient the fundamental (ω) polarization 40° with respect to its extraordinary axis. In this case, the 2ω pulse is linearly polarized along the

extraordinary axis whereas the ω pulse is elliptically polarized due to the birefringence of the BBO crystal. At the focal spot, a plasma filament of ~4 cm long is created. The THz pulses emitted from the plasma are focused by a pair of off-axis parabolic mirrors into a 1-mm thick zinc telluride (ZnTe) crystal for electro-optic (EO) sampling with synchronous probe pulses. A 3-mm thick silicon filter is inserted before the ZnTe crystal to block any unwanted optical light. By rotating the probe polarization together with the ZnTe crystal, we can characterize the THz fields projected onto two orthogonal (horizontal or vertical) axes of the lab frame. A broadband THz polarizer is placed before the ZnTe crystal for a better polarization analysis.

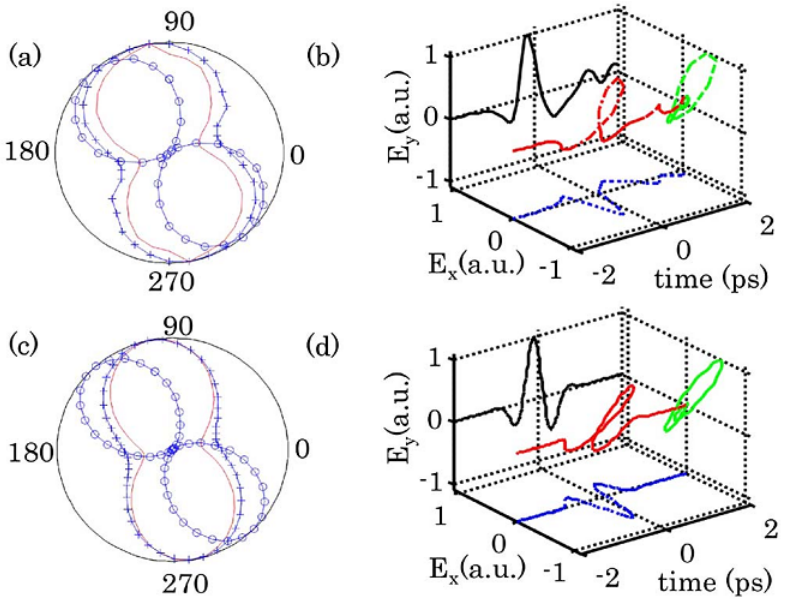

Figure 5.3 Elliptically polarized THz pulse generated by elliptically polarized ω and linearly polarized 2ω pulses. (a) Polarization maps of ω (red solid line) and 2ω pulses before (blue line with circles) and after (blue line with crosses) filamentation. (b) Measured THz fields: *x*-(blue) and *y*-(black) components with combined 3-dimensional (red) and projected (green) fields. (c),(d) Simulation results.

5.5 Results

We first characterize the polarization of ω and 2ω by placing and rotating a polarizing analyzer. Figure 5.3(a) shows the polarization maps of ω (red line), 2ω immediately after the BBO crystal (blue line with circles), and 2ω after propagating through the plasma (blue line with crosses). It shows that the ω pulse is elliptically polarized whereas the 2ω pulse is initially linearly polarized but becomes strongly elliptical after propagating through the plasma. The resulting THz is also elliptically polarized as shown in Figure 5.3(b).

To study how an elliptical THz pulse emerges from its propagation in plasma, we placed and scanned a pinhole aperture with 2 mm diameter along the plasma to control the effective plasma length contributing to the collected THz energy [88]. This blocks the THz emitted before the aperture while not affecting the THz emitted after the aperture. By scanning the aperture along the filament direction, we can control the plasma length responsible for the collected THz energy. Figure 5.4 shows the change in THz polarization for different effective plasma lengths. With a short plasma length, the measured THz pulse is linearly polarized with weaker output energy, as expected from the single-atom model. However, with increasing plasma length, the polarization evolves from linear to elliptical. Simultaneously, the THz amplitude increases with the major axis being slightly rotated counterclockwise. These phenomena can be understood as linearly polarized THz wavelets emitted from the local part of plasma superpose each other with a time difference due to the speed mismatch of optical and THz pulses. With $\Delta I_\omega = 3.3 \times 10^{13}$ W/cm^2 and $n_2 = 7.4 \times 10^{20}$

cm^2/W [89], we estimate $\Delta\phi_{2\omega}$ = 1.55 rad for a 4-cm long plasma. This calculation reproduces well the measured polarization state of 2ω as shown in Figure 5.3(a).

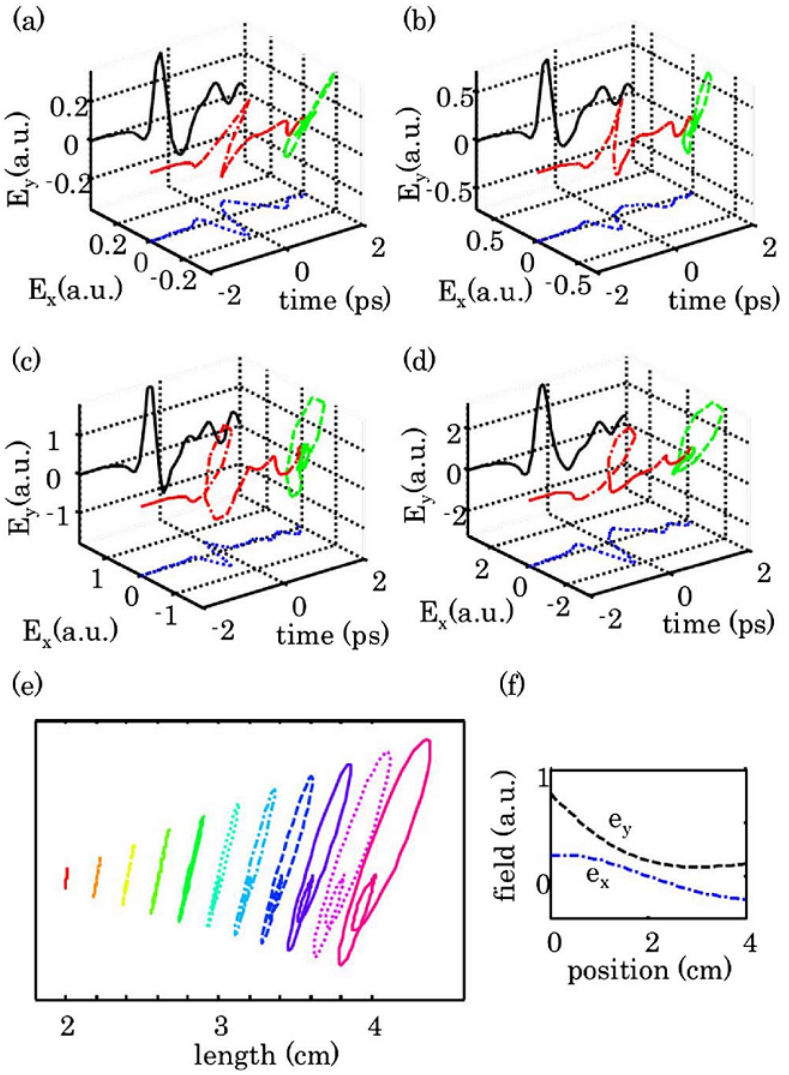

Figure 5.4 Measurements of conversion from linear to elliptical THz polarization with increasing effective plasma filament length: (a) 2.2 cm, (b) 2.8 cm, (c) 3.4 cm, and (d) 4.0 cm. (e) Simulated THz polarization change with increasing propagation length. (f) Simulated peak THz amplitudes along the *x* and *y* axes as a function of position *z'*.

By applying the parameters above, one can fully characterize the laser fields along the plasma, and the corresponding local THz fields can be calculated by the plasma current model. For instance, Figure 5.4(f) shows the local THz peak fields projected on both *x* and *y* axes, which vary along the plasma direction. Using Eq.

(5.7), with $\Delta n = 7 \times 10^{-4}$, the simulated THz pulse well reproduces the measured one [see Figure 5.3(b) and 5.3(d)]. We also calculate the change in THz polarization with varying plasma lengths. The result shown in Figure 5.4(e) fairly reproduces the measured THz polarization rotation and its transformation from linear to elliptical shown in Figure 5.4(a-d).

5.6 Conclusion

In summary, we report the mechanism of elliptically polarized THz pulse emission from two-color laser-produced plasma. The understanding presented here can be extended to other types of line sources which have a significant speed mismatch between the pump and generated pulses, consequently resulting in polarization-varying far-field radiation.

Appendix A: THz Sources and Detectors

A.1 THz sources

A.1.1 Continuous THz sources

Unlike pulsed THz sources which mainly rely on ultrafast laser techniques, continuous THz sources use many different types of technology. These technologies have been developed for a long time and continually pushed toward the THz frequency region either from infrared or microwave regime.

Far-infrared gas lasers are considered as one of the earliest sources for THz radiation. The gain mediums of those lasers are molecular gases such as ammonia and methanol where their rotational transition frequency lies in the THz frequency region. Usually those molecular gases are filled in a long resonant cavity (~1 meter) and pumped by optical waves or high electric fields. The efficiency in general is low and the radiation wavelengths are limited. Another type of continuous wave (cw) THz source is P-type germanium lasers which are electrically-pumped solid state lasers [90]. The gain medium is a germanium crystal doped with beryllium. The crystal is placed between a pair of strong magnets and biased by a high voltage electric field. The frequency is tunable from 1 to 4 THz by adjusting the electric and magnetic field strengths. This system, however, requires cryogenic cooling.

Compared to those bulky far-infrared lasers, quantum cascade lasers (QCLs), semiconductor heterostructure lasers [91], are compact and highly efficient. The QCL are a relatively new technique demonstrated in 1994 with lasing frequencies at mid-infrareds at first, and continuously pushed toward the THz frequency region over the past decades. The structure of QCLs consists of alternating layers of semiconductors

with thickness of only few atoms. These alternating layers create a set of potential wells. When a biased field is applied, it induces transitions down the energy wells where the electrons jump from higher quantum states to lower ones, simulating a "waterfall" effect. This cascading process emits photons with energies lying between the states, which can be tuned at THz frequencies.

CW THz waves can be also generated via difference frequency generation [92]. In this process, two optical beams with frequencies at ω_1 and ω_2 are mixed together in a nonlinear crystal, which emits radiation at the beat frequency $\omega_t = \omega_2 - \omega_1$ tuned at THz frequencies. Photomixing is a similar process which can generate THz radiation with the nonlinear crystal being replaced by a photoconductive switch [93]. In the process, THz frequency beating on a photoconductive antenna produces an oscillating current which emits cw THz radiation.

A.1.2 Pulsed THz sources

Pulsed (or broadband) THz pulse generation is similar to photomixing or difference frequency generation described in the previous section. Instead of being pumped by cw lasers, nonlinear crystals or photoconductive antennas are pumped by ultrashort (typically <100 fs) laser pulses. Due to their coherent and broadband nature of ultrashort pulses, the generated THz pulses are very short (~1 ps) approaching a near half-cycle oscillation.

One widely-used ultrashort pulsed laser uses titanium-doped aluminum oxide (Ti:sapphire) as a gain medium. This Ti:sapphire crystal has a broad gain spectrum, ranging from 650 nm to 1100 nm. Due to its high thermal conductivity, the crystal

can withstand high optical pumping power with scalable output power. Usually, the crystal is pumped by diode-pumped solid-state lasers operating at a wavelength of 532 nm, with stimulated emission near 800 nm. To produce ultrashort laser pulses, a mode-locking technique is required. In principle, a fixed phase relationship between the modes of the laser cavity yields interference in the time domain, producing a train of pulses. This mode locking can be achieved by an optical Kerr effect in the crystal (Kerr lens mode locking). Our Kerr-lens, mode-locked oscillator used for the experiments herein can produce ~10 *fs* (limited by dispersion) pulses with a few nano-joules at an 80 MHz repetition rate.

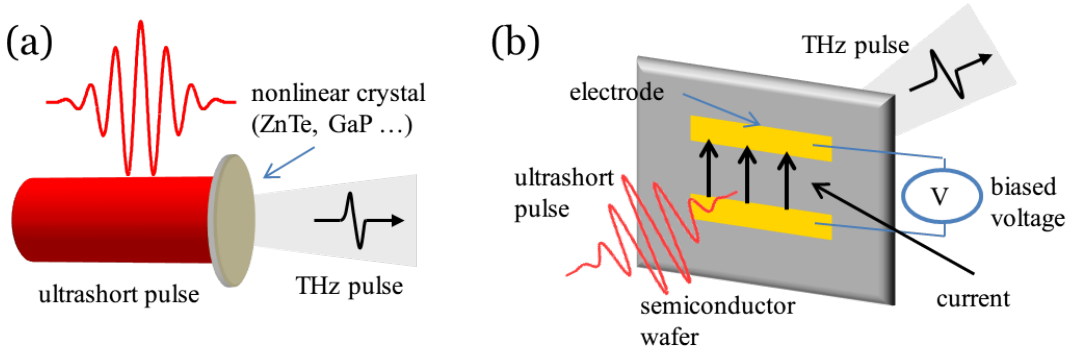

Figure A.1 Broadband THz pulse generation by (a) optical rectification and (b) photoconductive antenna.

Further energy (or power) amplification can be achieved by a chirped pulse amplification (CPA) technique, first developed by Mourou's group during the 1980s [94]. In this scheme, the output beam from a Ti:sapphire oscillator is seeded in a series of gain media, with its pulse duration stretched to hundreds of picosecond by a grating-based pulse stretcher. This lowers the peak power of amplified pulses and avoids any optical damage in the gain media. In practice, amplification is achieved in either regenerative or multi-pass amplifier, or a combination of both. After

amplification, a pulse compressor composed of gratings or prisms reduce the pulse duration back to the original one (<100 *fs*), thus enhancing the peak power.

A.1.2.1 Nonlinear crystals

One common method for THz pulse generation is using optical rectification [95]. Optical rectification is a second-order nonlinear process in which quasi-dc polarization is induced by an ultrashort pulse propagating through a material. Here, the second-order polarization $\tilde{P}^{(2)}$ can be expressed as $\tilde{P}^{(2)} = \chi^{(2)}\tilde{E}(t)^2$, where $\chi^{(2)}$ is the second-order susceptibility and $\tilde{E}(t)$ is the electric field of the incoming laser pulse. The electric field of an ultrashort laser pulse with central frequency ω can be written as $\tilde{E}(t) = E_0(t)e^{i\omega t} + \text{c.c}$, where $E_0(t)$ is the envelope of the laser pulse. Then $\tilde{P}^{(2)}$ can then be expressed as

$$\tilde{P}^{(2)} = 2\chi^{(2)}\left|E_0(t)\right|^2 + (\chi^{(2)}E_0(t)e^{i2\omega t} + \text{c.c}). \qquad \text{(A.1)}$$

The first term represents optical rectification whereas the second term denotes second harmonic generation, as shown by the frequency terms zero and 2ω. As shown in Eq. (A.1), the rectified nonlinear polarization arises over the laser pulse duration. This temporal modulation emits a THz pulse [96]. Although the equation suggests that the resulting THz pulse duration is similar to that of the input laser pulse, phase-matching and absorption in the crystal can limit the ultimate THz pulse duration.

Since optical rectification is a second-order nonlinear process, this process can only occur in a non-centrosymmetric crystal such as zinc telluride (ZnTe), lithium niobate ($LiNbO_3$), gallium selenide (GaSe), gallium arsenide (GaAs), and gallium phosphide (GaP). ZnTe is the most widely used crystal for THz generation because the group refractive index of ZnTe at 800 nm is matched with the refractive index at

THz frequencies. This naturally satisfies phase-matching and provides good conversion efficiency for THz generation.

A.1.2.2 Photoconductive antenna

Another way of generating THz pulses is to irradiate femtosecond pulses onto a biased photoconductive antenna [97]. Figure A.1 (b) shows a diagram for such a scheme. A photoconductive antenna consists of two electrodes deposited on a semiconductor substrate. Usually the gap between the electrodes is few micrometers, and a bias voltage around 40 V is applied between them. Femtosecond pulses with photon energies larger than the band gap of the semiconductor generate free electrons and holes in the electrode gap. Then the static bias field accelerates the free charge carriers, radiating sub-picosecond THz pulses.

Typically the output power scales linearly with the bias voltage and the optical pump power. However, the maximum biasing voltage is limited to ~100 V across a few microns distance because of electric discharge. In addition, the output power saturates with dense photocarriers, which can screen the bias field. The usual THz field strength generated by a photoconductive antenna is in the range of few kV/cm.

A.1.2.3 Review

Optical rectification and photoconduction are two most common methods used for THz pulse generation with table-top laser systems. Such sources provide THz fields on the order of kV/cm. One approach to scale up THz yields in both methods is using more intense laser pulses. However, this approach is fundamentally limited by material damage arising from two-photon or multi-photon absorption in nonlinear crystals and photoantennas. Another drawback is that THz output

bandwidths are limited by material dispersion and absorption. For example, phonon resonances in nonlinear crystals lie at 5 ~ 10 THz [98], strongly absorbing THz waves produced at those frequencies.

Other THz sources such as free electron lasers [99] and synchrotrons have been utilized to produce very strong THz fields with broad spectral tunability, but these facilities are large, expensive and less accessible than tabletop sources. By contrast, laser-produced plasmas [69] have been demonstrated as a promising compact high-power THz source. More details are provided in Chapter 1.

A.2 THz detection

A.2.1 Incoherent THz detection

Most incoherent THz detectors measure incident THz energy or power by measuring a temperature change induced by THz absorption. Such detectors include bolometers, Golay cells and pyroelectric detectors. Here we briefly describe the basic principles of their THz detection.

A bolometer has an electrical resistance thermometer to measure temperature changes induced by THz radiation. The materials are usually highly doped semiconductors such as Si or Ge whose electric resistance is sensitive to temperature. Typically bolometers require cryogenic cooling at or below liquid helium temperature for efficient detection.

In Golay cells, the radiation absorber is a blackened thin metal film. Absorbed THz radiation heats up the absorber, increasing the pressure of a gas filled in a chamber. The pressure deforms a flexible mirror placed behind the chamber. The

deformation is then detected by an optical beam reflected from the mirror, which measures the incident THz energy.

Pyroelectric detectors utilize pyroelectric materials which generate a voltage when they are heated or cooled. This pyroelectric effect arises from spontaneous electric polarization induced by temperature changes. Lithium tantalate (LiTaO3) is the most adapted material as pyroelectric detectors for THz detection.

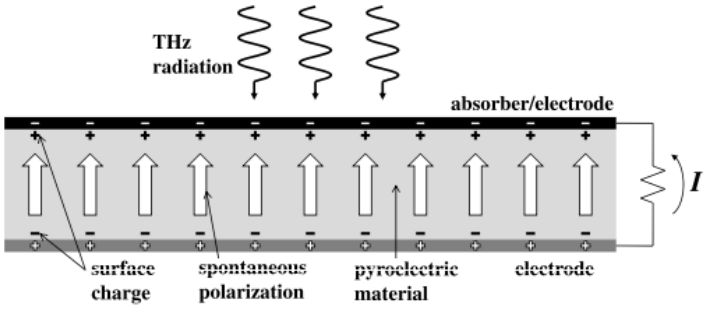

Figure A.2 Schematic diagram of a pyroelectric detector.(reprinted from [1])

Figure A.2 shows a typical scheme for pyroelectric detection. A pyroelectric material is sandwiched between two electrodes forming a capacitor. The top one is usually blacken to absorb incident radiation effectively. THz radiation directed to the detector heats up the absorber. A temperature rise in the pyroelectric material changes the polarization and simultaneously the surface charge. Then a current flows from the other electrode to compensate the loss of surface charge. Pyroelectric detectors are typically used in AC modes; usually a chopper is used to modulate incident THz power at 10~30 Hz.

Various filters can be used to characterize incident THz spectrum. For example, a silicon wafer can block optical light but transmit THz radiation with wavelengths of 1.2 μm to 1000 μm. Teflon or HDPE acts as a low-pass filter blocking THz frequencies higher than 3 THz.

A.2.2 Coherent THz detection

Coherent THz detection can be realized by a reverse process of coherent THz generation described in the previous section. Here we discuss broadband THz detection using nonlinear crystals or photoconductive antennas. Both methods can characterize THz electric fields in the time-domain, providing high-precision amplitude and phase measurements. A combination of coherent THz generation and detection constitutes THz time-domain spectroscopy.

A.2.2.1 Free-space electro-optic sampling

Free-space electro-optic (EO) sampling (EOS) was first demonstrated by Wu *et al*. in 1995 [55]. The underlying mechanism relies on the Pockels effect in an electro-optic crystal, a second-order nonlinear effect described as

$$P_i^{(2)}(\omega) = 2\sum_{j,k} \epsilon_0 \chi_{i,j,k}^{(2)}(\omega, \omega, 0) E_j(w) E_k(0), \tag{A.2}$$

where $\chi_{i,j,k}^{(2)}$ is the second-order susceptibility tensor. A static field $E_k(0)$ applied across the crystal induces birefringence, proportional to the applied field amplitude. By measuring the birefringence experienced by a probe beam $E_j(w)$, one can deduce the applied field strength.

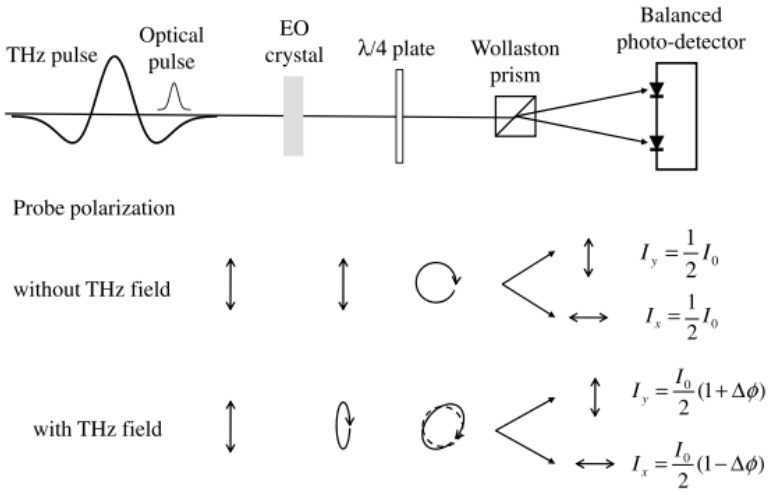

Figure A.3 Schematic diagram of free-space electro-optic sampling. (reprinted from [1])

Figure A.3 shows a schematic diagram for a typical EOS setup. In the case where there is no THz pulse, a linearly polarized optical pulse propagates through an EO crystal with no polarization change, and then the polarization becomes circular after a quarter waveplate. A Wollaston prism splits the circularly polarized probe into *p* and *s* polarized beams. A balanced photo-detector measures the intensity difference of these two beams. When a THz pulse co-propagates with the optical probe into the EO crystal, the THz field E_{THz} acts as a static field and induces a Pockels effect, making the probe beam elliptically polarized. Here, the phase difference $\Delta\phi$ between *s* and *p* polarization can be expressed as

$$\Delta\phi = \frac{\omega l}{c} n_O^3 r_{41} E_{THz}, \tag{A.3}$$

where n_O^3 is the refractive index at the optical frequency ω and r_{41} is the EO coefficient. The intensities of *s* and *p* components at the balanced detector can be expressed as $I_s \sim \frac{I_0}{2}(1-\Delta\phi)$ and $I_p \sim \frac{I_0}{2}(1+\Delta\phi)$, where I_0 is the intensity of the

probe beam. Here, the balanced detector measures the intensity difference ΔI between these two components, which is $\Delta I = I_y - I_x = I_0 \Delta\phi$. Since $\Delta\phi \propto E_{THz}$, the balanced detector signal measures the THz amplitude. By scanning the delay between the probe and THz pulses, one can map out the entire THz waveform.

Similar to the generation case, the detectable bandwidth depends on phase-matching and absorption in the EO crystal. In general, a thick EO crystal provides a large EOS signal but its detection bandwidth is limited by phase-matching in the crystal. In addition, THz absorption at 5 ~ 10 THz due to transverse-optical phonon resonances in an EO crystal can further reduce its detection bandwidth.

A.2.2.2 Photoconductive antenna

In the last section, we introduced THz generation with photoconductive antennas. A reverse process can be utilized to detect coherent THz fields. In an unbiased photoconductive antenna, an optical probe beam with photon energy greater than the band gap of the substrate excites photocarriers in the substrate. An incoming THz pulse focused on the antenna accelerates the photocarriers and forms a current. The current can be amplified by a current amplifier and detected by an ammeter. By varying the delay between the optical and THz pulses, THz waveforms can be characterized in the time-domain. Here, the measured current is proportional to the incoming THz field. The detection bandwidth, however, is limited by the conductivity of the substrate and the probe pulse duration.

Bibliography

[1] Y. S. Lee, *Principles of Terahertz Science and Technology* (Springer, USA, 2008).

[2] B. Ferguson and X.-C. Zhang, Nat. Mater. **1**, 26 (2002).

[3] M. Tonouchi, Nat. Photonics **1**, 97 (2007).

[4] M. van Exter, C. Fattinger, and D. Grischkowsky, Opt. Lett. **14**, 1128 (1989).

[5] D. M. Mittleman, M. Gupta, R. Neelamani, R. G. Baraniuk, J. V. Rudd, and M. Koch, Appl. Phys. B **68**, 1085 (1999).

[6] S. Fleischer, Y. Zhou, R. W. Field, and K. A. Nelson, Phys. Rev. Lett. **107**, 163603 (2011).

[7] B. Born, S. J. Kim, S. Ebbinghaus, M. Gruebele, and M. Havenith, Faraday Discuss. **141**, 161 (2009).

[8] J. Ahn, D. Hutchinson, C. Rangan, and P. Bucksbaum, Phys. Rev. Lett. **86**, 1179 (2001).

[9] H. G. Roskos, Phys. Scr. **T86**, 51 (2000).

[10] C. A. Schmuttenmaer, Chem. Rev. **104**, 1759 (2004).

[11] R. Ulbricht, E. Hendry, J. Shan, T. Heinz, and M. Bonn, Rev. Mod. Phys. **83**, 543 (2011).

[12] H. Hamster, A. Sullivan, S. Gordon, W. White, and R. Falcone, Phys. Rev. Lett. **71**, 2725 (1993).

[13] J. R. Cary and A. N. Kaufman, Phys. Fluids 1958-1988 **24**, 1238 (1981).

[14] W. P. Leemans, C. G. R. Geddes, J. Faure, C. Tóth, J. van Tilborg, C. B. Schroeder, E. Esarey, G. Fubiani, D. Auerbach, B. Marcelis, M. A. Carnahan, R. A. Kaindl, J. Byrd, and M. C. Martin, Phys. Rev. Lett. **91**, 074802 (2003).

[15] T. Löffler, F. Jacob, and H. G. Roskos, Appl. Phys. Lett. **77**, 453 (2000).

[16] A. Houard, Y. Liu, B. Prade, V. T. Tikhonchuk, and A. Mysyrowicz, Phys. Rev. Lett. **100**, 255006 (2008).

[17] D. J. Cook and R. M. Hochstrasser, Opt. Lett. **25**, 1210 (2000).

[18] T. Bartel, P. Gaal, K. Reimann, M. Woerner, and T. Elsaesser, Opt. Lett. **30**, 2805 (2005).

[19] X. Xie, J. Dai, and X.-C. Zhang, Phys. Rev. Lett. **96**, 075005 (2006).

[20] T. I. Oh, Y. S. You, N. Jhajj, E. W. Rosenthal, H. M. Milchberg, and K. Y. Kim, New J. Phys. **15**, 075002 (2013).

[21] K. Kim, A. Taylor, J. Glownia, and G. Rodriguez, Nat Photon **2**, 605 (2008).

[22] M. D. Thomson, V. Blank, and H. G. Roskos, Opt. Express **18**, 23173 (2010).

[23] I. Babushkin, W. Kuehn, C. Köhler, S. Skupin, L. Bergé, K. Reimann, M. Woerner, J. Herrmann, and T. Elsaesser, Phys. Rev. Lett. **105**, 053903 (2010).

[24] I. Babushkin, S. Skupin, and J. Herrmann, Opt. Express **18**, 9658 (2010).

[25] E. Matsubara, M. Nagai, and M. Ashida, Appl. Phys. Lett. **101**, 011105 (2012).

[26] P. Corkum, Phys. Rev. Lett. **71**, 1994 (1993).

[27] L. V. Keldysh, Sov. Phys. JETP **20**, 1307 (1965).

[28] M. V. Ammosov, N. B. Delone, and V. P. Kraĭnov, Sov. Phys. - JETP **64**, 1191 (1986).

[29] D. J. Cook and R. M. Hochstrasser, Opt. Lett. **25**, 1210 (2000).

[30] K.-Y. Kim, J. H. Glownia, A. J. Taylor, and G. Rodriguez, Opt. Express **15**, 4577 (2007).

[31] D. Zhang, Z. Lü, C. Meng, X. Du, Z. Zhou, Z. Zhao, and J. Yuan, Phys. Rev. Lett. **109**, 243002 (2012).

[32] A. N. Chudinov, Y. E. Kapitzky, A. A. Shulginov, and B. Y. Zel'dovich, Opt. Quantum Electron. **23**, 1055 (1991).

[33] D. W. Schumacher, F. Weihe, H. G. Muller, and P. H. Bucksbaum, Phys. Rev. Lett. **73**, 1344 (1994).

[34] R. Stolle, G. Marowsky, E. Schwarzberg, and G. Berkovic, Appl. Phys. B **63**, 491 (1996).

[35] R. W. Boyd, *Nonlinear Optics*, 3rd ed. (Academic Press, 2008).

[36] M. Li, W. Li, Y. Shi, P. Lu, H. Pan, and H. Zeng, Appl. Phys. Lett. **101**, 161104 (2012).

[37] T. Balciunas, A. J. Verhoef, A. V. Mitrofanov, G. Fan, E. E. Serebryannikov, M. Y. Ivanov, A. M. Zheltikov, and A. Baltuska, Chem. Phys. **414**, 92 (2013).

[38] B. Edlén, Metrologia **2**, 71 (1966).

[39] L. Bergé, S. Skupin, C. Köhler, I. Babushkin, and J. Herrmann, Phys. Rev. Lett. **110**, 073901 (2013).

[40] A. V. Borodin, N. A. Panov, O. G. Kosareva, V. A. Andreeva, M. N. Esaulkov, V. A. Makarov, A. P. Shkurinov, S. L. Chin, and X.-C. Zhang, Opt. Lett. **38**, 1906 (2013).

[41] F. Théberge, M. Châteauneuf, G. Roy, P. Mathieu, and J. Dubois, Phys. Rev. A **81**, 033821 (2010).

[42] T. Fuji and T. Suzuki, Opt Lett **32**, 3330 (2007).

[43] D. Côté, J. M. Fraser, M. DeCamp, P. H. Bucksbaum, and H. M. van Driel, Appl. Phys. Lett. **75**, 3959 (1999).

[44] J. Güdde, M. Rohleder, T. Meier, S. W. Koch, and U. Höfer, Science **318**, 1287 (2007).

[45] N. Dudovich, O. Smirnova, J. Levesque, Y. Mairesse, M. Y. Ivanov, D. M. Villeneuve, and P. B. Corkum, Nat. Phys. **2**, 781 (2006).

[46] D. Ray, F. He, S. De, W. Cao, H. Mashiko, P. Ranitovic, K. P. Singh, I. Znakovskaya, U. Thumm, G. G. Paulus, M. F. Kling, I. V. Litvinyuk, and C. L. Cocke, Phys. Rev. Lett. **103**, 223201 (2009).

[47] K. J. Betsch, D. W. Pinkham, and R. R. Jones, Phys. Rev. Lett. **105**, 223002 (2010).

[48] I. V. Litvinyuk, K. F. Lee, P. W. Dooley, D. M. Rayner, D. M. Villeneuve, and P. B. Corkum, Phys. Rev. Lett. **90**, 233003 (2003).

[49] D. Pavičić, K. F. Lee, D. M. Rayner, P. B. Corkum, and D. M. Villeneuve, Phys. Rev. Lett. **98**, 243001 (2007).

[50] H. Stapelfeldt and T. Seideman, Rev. Mod. Phys. **75**, 543 (2003).

[51] X. M. Tong, Z. X. Zhao, and C. D. Lin, Phys. Rev. A **66**, 033402 (2002).

[52] C. D. Lin and X. M. Tong, J. Photochem. Photobiol. Chem. **182**, 213 (2006).

[53] K. Y. Kim, Phys. Plasmas **16**, 056706 (2009).

[54] Z. X. Zhao, X. M. Tong, and C. D. Lin, Phys. Rev. A **67**, 043404 (2003).

[55] Q. Wu and X.-C. Zhang, Appl. Phys. Lett. **67**, 3523 (1995).

[56] H. Wen and A. M. Lindenberg, Phys. Rev. Lett. **103**, 023902 (2009).

[57] J. Dai, N. Karpowicz, and X.-C. Zhang, Phys. Rev. Lett. **103**, 023001 (2009).

[58] T. I. Oh, Y. S. You, and K. Y. Kim, Opt. Express **20**, 19778 (2012).

[59] Y.-H. Chen, S. Varma, A. York, and H. M. Milchberg, Opt. Express **15**, 11341 (2007).

[60] M. Fejer, G. Magel, D. Jundt, and R. Byer, Quantum Electron. IEEE J. Of **28**, 2631 (1992).

[61] X. Zhang, A. Lytle, T. Popmintchev, X. Zhou, H. Kapteyn, M. Murnane, and O. Cohen, Nat. Phys. **3**, 270 (2007).

[62] E. A. Gibson, A. Paul, N. Wagner, R. Tobey, D. Gaudiosi, S. Backus, I. P. Christov, A. Aquila, E. M. Gullikson, D. T. Attwood, M. M. Murnane, and H. C. Kapteyn, Science **302**, 95 (2003).

[63] A. Nahata, A. S. Weling, and T. F. Heinz, Appl. Phys. Lett. **69**, 2321 (1996).

[64] Y.-S. Lee, T. Meade, V. Perlin, H. Winful, T. B. Norris, and A. Galvanauskas, Appl. Phys. Lett. **76**, 2505 (2000).

[65] J. Fülöp, L. Pálfalvi, S. Klingebiel, G. Almási, F. Krausz, S. Karsch, and J. Hebling, Opt Lett **37**, 557 (2012).

[66] K. L. Yeh, M. C. Hoffmann, J. Hebling, and K. A. Nelson, Appl. Phys. Lett. **90**, 171121 (2007).

[67] C. D'Amico, A. Houard, M. Franco, B. Prade, A. Mysyrowicz, A. Couairon, and V. T. Tikhonchuk, Phys. Rev. Lett. **98**, 235002 (2007).

[68] H. Zhong, N. Karpowicz, and X. C. Zhang, Appl. Phys. Lett. **88**, 261103 (2006).

[69] K.-Y. Kim, J. H. Glownia, A. J. Taylor, and G. Rodriguez, Opt. Express **15**, 4577 (2007).

[70] M. Kress, T. Löffler, S. Eden, M. Thomson, and H. G. Roskos, Opt. Lett. **29**, 1120 (2004).

[71] A. Couairon and A. Mysyrowicz, Phys. Rep. **441**, 47 (2007).

[72] Y. Liu, A. Houard, M. Durand, B. Prade, and A. Mysyrowicz, Opt Express **17**, 11480 (2009).

[73] Y. H. Chen, S. Varma, T. M. Antonsen, and H. M. Milchberg, Phys. Rev. Lett. **105**, 215005 (2010).

[74] J. Morris and Y. Shen, Phys. Rev. A **15**, 1143 (1977).

[75] L. A. Johnson, J. P. Palastro, T. M. Antonsen, and K. Y. Kim, Phys. Rev. A **88**, 063804 (2013).

[76] F. Blanchard, G. Sharma, X. Ropagnol, L. Razzari, R. Morandotti, and T. Ozaki, Opt Express **17**, 6044 (2009).

[77] R. A. Akhmedzhanov, I. E. Ilyakov, V. A. Mironov, E. V. Suvorov, D. A. Fadeev, and B. V. Shishkin, J. Exp. Theor. Phys. **109**, 370 (2009).

[78] P. Klarskov, A. C. Strikwerda, K. Iwaszczuk, and P. U. Jepsen, New J. Phys. **15**, 075012 (2013).

[79] V. Blank, M. D. Thomson, and H. G. Roskos, New J. Phys. **15**, 075023 (2013).

[80] D. Dietze, J. Darmo, S. Roither, A. Pugzlys, J. Heyman, and K. Unterrainer, J Opt Soc Am B **26**, 2016 (2009).

[81] Y. Chen, C. Marceau, S. Génier, F. Théberge, M. Châteauneuf, J. Dubois, and S. L. Chin, Opt. Commun. **282**, 4283 (2009).

[82] J.-M. Manceau, M. Massaouti, and S. Tzortzakis, Opt. Express **18**, 18894 (n.d.).

[83] G. Rodriguez, A. R. Valenzuela, B. Yellampalle, M. J. Schmitt, and K.-Y. Kim, J. Opt. Soc. Am. B **25**, 1988 (2008).

[84] P. Béjot, Y. Petit, L. Bonacina, J. Kasparian, M. Moret, and J. Wolf, Opt Express **16**, 7564 (2008).

[85] O. Kosareva, N. Panov, V. Makarov, I. Perezhogin, C. Marceau, Y. Chen, S. Yuan, T. Wang, H. Zeng, A. Savel'ev, and S. Leang Chin, Opt. Lett. **35**, 2904 (2010).

[86] X. Lu and X.-C. Zhang, Phys. Rev. Lett. **108**, 123903 (2012).

[87] C. Marceau, S. Ramakrishna, S. Génier, T.-J. Wang, Y. Chen, F. Théberge, M. Châteauneuf, J. Dubois, T. Seideman, and S. L. Chin, Opt. Commun. **283**, 2732 (2010).

[88] Y. You, T. Oh, and K. Kim, Phys. Rev. Lett. **109**, 183902 (2012).

[89] J. K. Wahlstrand, Y. H. Cheng, and H. M. Milchberg, Phys. Rev. A **85**, 043820 (2012).

[90] A. Bergner, U. Heugen, E. Bründermann, G. Schwaab, M. Havenith, D. R. Chamberlin, and E. E. Haller, Rev. Sci. Instrum. **76**, 063110 (2005).

[91] J. Faist, F. Capasso, D. L. Sivco, C. Sirtori, A. L. Hutchinson, and A. Y. Cho, Science **264**, 553 (1994).

[92] W. Shi and Y. J. Ding, Appl. Phys. Lett. **84**, 1635 (2004).

[93] E. R. Brown, F. W. Smith, and K. A. McIntosh, J. Appl. Phys. **73**, 1480 (1993).

[94] D. Strickland and G. Mourou, Opt. Commun. **56**, 219 (1985).

[95] M. Bass, P. Franken, J. Ward, and G. Weinreich, Phys. Rev. Lett. **9**, 446 (1962).

[96] A. Rice, Y. Jin, X. F. Ma, X.-C. Zhang, D. Bliss, J. Larkin, and M. Alexander, Appl. Phys. Lett. **64**, 1324 (1994).

[97] J. T. Darrow, B. B. Hu, X.-C. Zhang, and D. H. Auston, Opt. Lett. **15**, 323 (1990).

[98] G. Gallot, J. Zhang, R. W. McGowan, T.-I. Jeon, and D. Grischkowsky, Appl. Phys. Lett. **74**, 3450 (1999).

[99] G. L. Carr, M. C. Martin, W. R. McKinney, K. Jordan, G. R. Neil, and G. P. Williams, Nature **420**, 153 (2002).

List of Publications

- T.I. Oh, **Y.S. You**, N. Jhajj, E.W. Rosenthal, H.M. Milchberg, and K.Y. Kim, "Intense terahertz generation in two-color laser filamentation: energy scaling with terawatt laser systems" New J. Phys. **15**, 075002 (2013).
- T. Oh, **Y. S. You**, N. Jhajj, E. Rosenthal, H. M. Milchberg, and K. Y. Kim "Scaling and Saturation of High-Power Terahertz Radiation Generation in Two-Color Laser Filamentation" Appl. Phys. Lett. **102**, 201113 (2013)
- **Y. S. You**, T. Oh, and K. Kim, "A mechanism of elliptically polarized terahertz generation in two-color laser filamentation", Opt. Lett. **38**, 1034, 2013
- **Y. S. You**, T. Oh, A.B. Fallahkahair, and K. Kim, "Alignment-Dependent Terahertz Radiation in Two-Color Photoionization of Molecules", Phys. Rev. A. **87**, 035401, 2013.
- **Y. S. You**, T. Oh, and K. Kim, "Off-axis phase-matched terahertz emission from two-color laser-induced plasma filaments", Phys. Rev. Lett. **109**, 183902, 2012.
- T. Oh, **Y. S. You**, and K. Kim, "Two-Dimensional Plasma Current and Optimized Terahertz Generation in Two-Color Photoionization", Opt. Express., **20** 19778-19786, 2012.